Science of the Total Environment 917 (2024) 170391

Contents lists available at ScienceDirect

Science of the Total Environment

journal homepage: www.elsevier.com/locate/scitotenv

Thermal photogrammetry on a permafrost rock wall for the active layer monitoring

Stefano Ponti [a,b,*], Irene Girola [a], Mauro Guglielmin [a,b]

[a] University of Insubria, via J.H. Dunant, 3, 21100 Varese, Italy
[b] Climate Change Research Center (CCRC), University of Insubria, via San Abbondio, 12, 22100 Como, Italy

HIGHLIGHTS

- UAV thermal photogrammetry has been used to model the active layer thickness (ALT) on a rock wall.
- Thermal inertia has been converted into ALT.
- Other models underestimate the ALT and the Alpine Permafrost Index Map (APIM) did not match with the ALT distribution.
- The ALT increase of 29.3 cm from 2021 to 2022 is caused by the variable snow accumulation on the rock wall.
- Possible rock mass wasting is expected as well as future changes of topography and ALT.

GRAPHICAL ABSTRACT

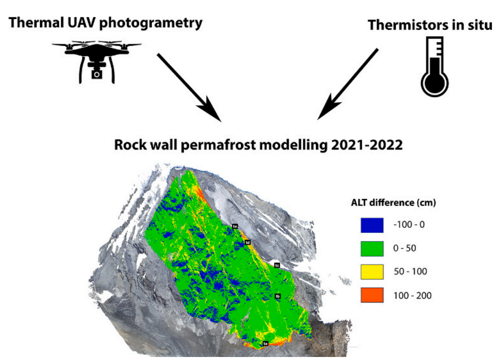

ARTICLE INFO

Editor: Martin Drews

Keywords:
Thermal photogrammetry
Rock wall
Permafrost
ALT modelling
Thermal inertia

ABSTRACT

Permafrost and active layer models often cannot explain the high spatial variability, especially in heterogeneous environments like the mountainous regions due to their scarce resolution, paucity of climatic data and topographic details. In this study, we want to introduce a new application of the unmanned aerial vehicle (UAV) in thermal photogrammetry to model the active layer thickness (ALT) of an alpine rock wall through the computation of the thermal inertia and compare the results with a widespread ALT model. On the Gran Zebrù South rock wall, 8 thermal UAV surveys has been conducted in 4 different summer days during 2021-2022 in order to have two 3D thermal models per day at different solar radiation inputs. By analyzing topographic data, visible imagery and the thermal models, the apparent thermal inertias (ATIs) have been converted into heat transfer coefficients (HTCs) and then into ALT of 2021 and 2022. These maps have been validated through the placement of thermistors at different elevations and with variable depths (2, 15 and 40 cm from the rock surface).

The resulting ALT has been compared with the Stefan's solution and the alpine permafrost index map (APIM), which showed large underestimations and a noncorrespondence with permafrost occurrence. The average ALT increase of 29.3 cm from 2021 to 2022 has been discussed regarding permafrost formation/degradation future trend under the climatic change and potential risks of alpine areas.

* Corresponding author at: University of Insubria, via J.H. Dunant, 3, 21100 Varese, Italy.
E-mail address: stefano.ponti@uninsubria.it (S. Ponti).

https://doi.org/10.1016/j.scitotenv.2024.170391
Received 2 September 2023; Received in revised form 11 January 2024; Accepted 21 January 2024
Available online 26 January 2024

1. Introduction

In the recent years, the climatic change impacts on high-altitude mountains have been high IPCC (IPCC, 2022). The European Alps underwent an increase of air temperature of 0.2–0.7 °C per decade during 2000–2019 (Etzelmüller et al., 2020), that is largely higher than the world average (Pepin et al., 2015). Also, the solid precipitation trend is decreasing with effects on the accumulation and duration of the snow cover, especially at high elevations in the Alps (Kotlarski et al., 2023; Marty et al., 2017). These parameters are two of the most important drivers for the permafrost occurrence and weathering processes, especially in alpine areas (Draebing et al., 2017). In the European Alps permafrost occurrence is thought to be probable above 2500 m a.s.l. (Oliva et al., 2018), where the landscape is majorly composed of bare grounds/rocks or rock walls. In these high-elevations, periglacial processes are widespread (Draebing et al., 2022) and, coupled with the permafrost degradation (Biskaborn et al., 2019; Etzelmüller et al., 2020; Guglielmin et al., 2021a), increase the slope instability leading to hazards and risks (Bommer et al., 2010; Duvillard et al., 2021b, 2019). Permafrost degradation on the Alps has been demonstrated through boreholes (Guglielmin et al., 2018; Etzelmüller et al., 2020), physical modelling (i.e., Etzelmüller et al., 2022) geophysical soundings (Buckel et al., 2022; Duvillard et al., 2021a; Etzelmüller et al., 2020; Guglielmin et al., 2021b). Remote sensing (unmanned aerial vehicles (UAVs) or satellites) has been largely used to detect/map the expression of permafrost through surface characteristics (Jones et al., 2021; Jorgenson and Grosse, 2016; Obu et al., 2020, 2019; Samsonov et al., 2016). Unfortunately, UAV remote sensing advances rely only on the visible effect of permafrost presence on the ground surface (Fraser et al., 2015; van der Sluijs et al., 2018) rather than investigate its thermal conditions. On the Alps, only the Alpine Permafrost Index Map (APIM) topo-climatic model (Boeckli et al., 2012) has been developed as good resolution model despite its old climatic series. It is also important to say that, in the European Alps, physical modelling of permafrost relies on digital terrain models (DTMs) which rarely exceed 5 m of resolution (Draebing et al., 2022) and are therefore inappropriate to represent very steep rock walls. Hence, the solution for detecting permafrost in alpine rock walls remains linked to the use of electrical resistivity tomography (ERT) on the rock walls (Duvillard et al., 2021a; Etzelmüller et al., 2022; Scandroglio et al., 2021) or thermistor chains in boreholes (Etzelmüller et al., 2020; Krautblatter et al., 2010; Magnin et al., 2015a; Magnin et al., 2017). However, these tools will never cover a sufficient number to extrapolate an entire rock wall.

It is for this reason that laser scanners or UAV photogrammetry are mandatory to have a detailed 3D topography of the rock walls that DTMs cannot reach; only UAVs guarantee a high accessibility to harsh areas (Kurdel et al., 2019). Moreover, the fact that the most advanced airborne cameras can provide multispectral sensor such as the thermal band (Forte et al., 2021; Santin et al., 2023) it is of enormous interest to assess the spatial variability of the surface temperature of rocks (Kraaijenbrink et al., 2018). In this sense, several studies were done concerning thermal photogrammetry that provides thermal 3D models or orthophotos (Bisset et al., 2022; Forte et al., 2021; Santin et al., 2023). It is well known that the surface temperature is a product of the surface energy balance and thus it is dependent on the wind, air temperature, snow cover, surficial moisture (e.g. Oke, 1987; Guglielmin et al., 2003). Therefore, apparently it is hard to relate the surface temperature with the thermal profile, namely permafrost. However, different timing of acquisition of surface temperatures can provide information about the thermal characteristics of deep layers, for example with the calculation of the thermal inertia that has been addressed to permafrost detection (Bandfield and Feldman, 2008; Nixon, 1990). Thermal inertia calculated from UAV thermal imagery has been used for surficial soil water content (Maltese et al., 2010; Minacapilli et al., 2012), but never for detecting cryotic conditions on Earth. We therefore sustain that the presence of a shallow permafrost table (that is a thin active layer thickness, ALT) would physically alter the vertical propagation of surface heat to the interior, thus being an indicator of the ALT. In this paper, we therefore aim to use a thermal inertia-based index obtained via thermal photogrammetry to detect the rock wall ALT by using UAV thermal imagery, understand the ALT change between 2021 and 2022, compare it with other models and draw future consequences about the South Gran Zebrù peak rock wall.

2. Study area

This studied area is situated in the Ortles-Cevedale group (Central Italian Alps, Italy). The Ortles-Cevedale group is the largest glacierized mountain group of the Italian Alps and is undergoing rapid glacier shrinkage (D'Agata et al., 2014). The object of the study is the Gran Zebrù peak (3857 m a.s.l.) and in particular its southern face, that rises from the top of the Gran Zebrù Eastern glacier tongue (ca. 3300 m a.s.l.) until the summit (Fig. 1). The choice of this summit arises also from the fact that in 2003 the Thurwieser peak (at ca. 2 km Northwest from the Gran Zebrù) underwent a big rock avalanche induced by permafrost thawing (Pirulli, 2009) on his southern slope.

The Gran Zebrù southern rock wall is composed of carbonatic rocks (dolomite and limestone) with intercalations of fine black limestones (Forte et al., 2021; Montrasio et al., 2012). Furthermore, in the area, there is an important tectonic lineament (Gran Zebrù Thrust) that is still seismically active (Albini et al., 1994).

The area is characterized by a continental Alpine climate (Soncini et al., 2016). Annual precipitation is about 850 mm (40 % falling from June to August) (Leonelli et al., 2017). At the Gran Zebrù Eastern Glacier (3170 m a.s.l.) level the mean annual air temperature (2010−2020) is −2.2 °C, while the total snow accumulation for the hydrological year 2019/2020 is averagely 0.2 m of water equivalent. The mean summer air temperature (JJA) at the same elevation for the same period 2010–2020 is 5.0 °C (Forte et al., 2021).

The average rock wall slope is 46°, while the aspect 177°.

3. Material and methods

3.1. Temperature loggers

During summer 2021, 5 temperature logger sites were installed on the rock wall at different altitudes: each site consisted of one uncalibrated Onset HOBO U23 (0.2 °C of accuracy) logger with 2 thermistors installed at 2 cm of depth from the rock surface (Ponti et al., 2021b) with the help of a portable electric driller. The sites choice was based on the interpretation of the first drone thermal survey: only the snow-free rock faces with surface temperature between 0 and − 7 °C were chosen to increase the probability of permafrost occurrence. The 2 channels that composed each logger were installed at the same elevation and at the same aspect and slope as replicate records. Where possible, a similar configuration of aspect and slope was maintained also at the other loggers' sites except for their elevation. The loggers were set to record every 30 min from 22/08/2021 to 12/10/2022. A summary of the loggers' settings is shown in Table 1.

In Te, the 2 thermistors were placed at 2 and 15 cm of depth in order to have a rock depth thermal gradient useful to calculate the 0 °C isotherm as indicator of the ALT (Guglielmin, 2006). It is true that 2 and 15 cm of depth are not the best choice for the thermal profile extrapolation, but the harsh conditions of the rock wall permitted the operator to carry only a small driller. A deeper borehole was then drilled in Ta thank to its accessibility. There, besides the couple of 2 cm thermistors, a deeper borehole equipped with thermistors in a PVC tube at 2, 15 and 40 cm of depth was installed. Unfortunately, due to a small debris fall, these last thermistors were damaged in 2021 and thus replaced in 2022, permitting the start of logging since 04/08/2022. Likewise, due to the very dangerous conditions of the rock wall, it has not been possible to collect the Tb logger and download its data. An example (Tb) of the

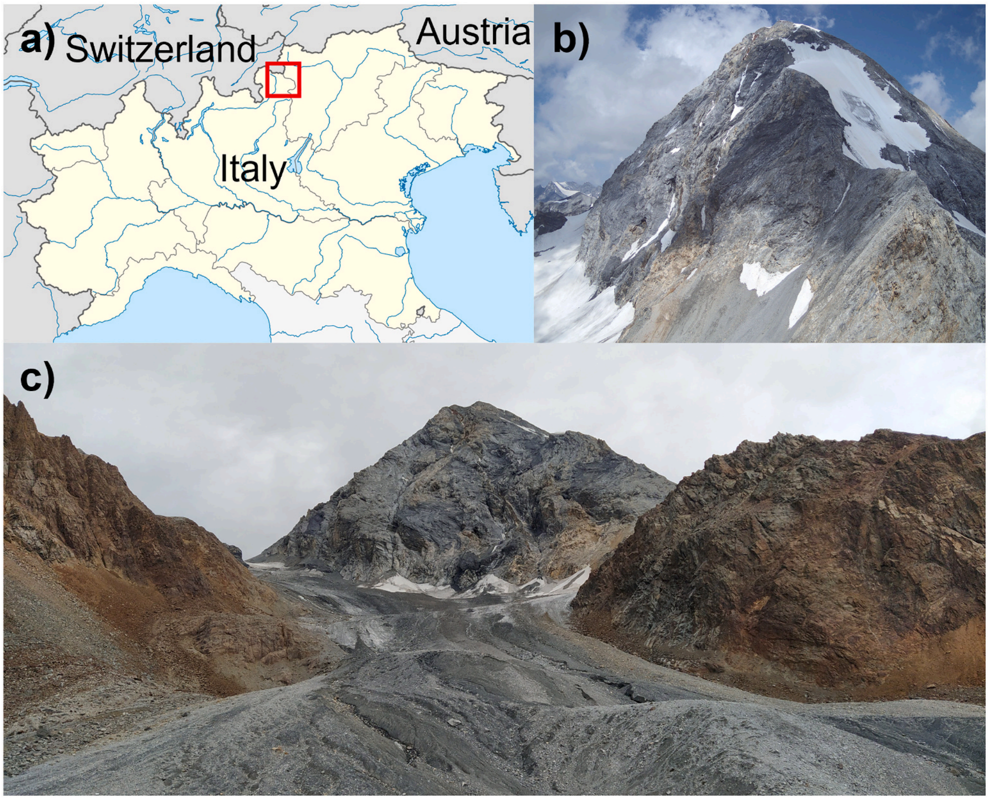

Fig. 1. Location of the Gran Zebrù peak in Upper Valtellina (Central Alps) (a). Details of the South rock wall taken on the 23/07/2021 next to the SE ridge (from drone above the eastern tongue of the Granz Zebrù glacier) (b) and on the 14/07/2022 from the ground at the glacier forefield of the glacier southern tongue (c).

Table 1
Topographic characterization of the sites where the thermistors were placed.

Loggers' site	Elevation (m a.s.l.)	Mean slope (°)	Mean aspect (°)	Borehole depth (cm)
Ta	3230	85	145	40
Tb	3360	55	185	2
Tc	3470	44	198	2
Td	3570	47	125	2
Te	3655	48	160	15

experimental setup is shown in Fig. 2.

3.2. UAV survey

The photogrammetric acquisition of the summit rock face consisted of several manual UAV flights conducted with a DJI Matrice 210 v2 RTK, that permitted a geotag information per RGB picture with an accuracy of 2 cm. The portable base station was placed at 3050 m a.s.l., close to the automatic weather station at the glacier front (AWS) (Forte et al., 2021). The choice of the surveys' dates was based on the melting of the snow cover from the rock face and the bottom glacier (usually in late July) and before the beginning of the snow season (usually late September). Even though the manual flight is not recommended, the operator manually followed a flight pattern that is similar to the nadiral surveys typical in photogrammetry but conducted vertically and with oblique acquisitions respect to the rock wall (Mineo et al., 2022), trying to maintain the same distance to the rock wall (ca. 300 m) that provided a ground sample distance (GSD) of 7 cm for RGB and 28 cm for the thermal band. The mounted camera was a DJI Zenmuse XT2, able to acquire both RGB images at 12 MP (8 mm of focal length) and thermal (640 × 512 pixels at 7–13.5 μm bandwidth) images (19 mm of focal length) with an accuracy of absolute temperatures of 2.0 °C and a resolution of 0.1 °C. The time-interval of the image acquisition was set every 2 s to guarantee a good overlap between couples of pictures both for the visible and the thermal sensor (>60 %). The total number of pictures taken depended on the flight duration and ranged between 253 (23/07/2021) and 547 (22/07/2022) images per both RGB and thermal bands. The main objective of the UAV surveys was to operate both at the minimum and at the maximum of the solar incoming radiation/surface temperature in order to calculate the apparent thermal inertia (ATI) (Maltese et al., 2010; Minacapilli et al., 2012; Verstraeten et al., 2006) of the rock wall. The experimental design permitted to compare the ATI at the beginning and end of the snow-free season for 2022 and 2021. The 23/07/2021 point cloud details have been shown but not utilized for the analysis because it was much smaller than the whole rock wall due to the limited number of photograms. Moreover, because of the logistic effort and the rapidly changing weather conditions, not all the surveys were conducted at the absolute maximum and minimum rock surface temperature (RST), keeping in mind that in this alpine region the minimum surface temperature is reached just before the sunrise (Ponti et al., 2018). However, at the closest AWS the incoming solar radiation (W m^{-2}) and ground surface temperature (°C) maxima and minima well resembled all the surveys' span of time (Table 2).

The calibration of the thermal images was computed via linear regression with the most surficial thermistors ($R^2 > 0.72$, $p < 0.01$), therefore, since the relative temperatures were more important and accurate than the absolute temperatures, the emissivity value of the rock surface was negligible and kept to 1.0 (Heinl et al., 2012; Kraaijenbrink et al., 2018).

3.3. Data analysis

3.3.1. Temperature analyses

At the thermistors locations, and based on the hydrological year 2021–2022, it was calculated the mean annual rock surface temperature

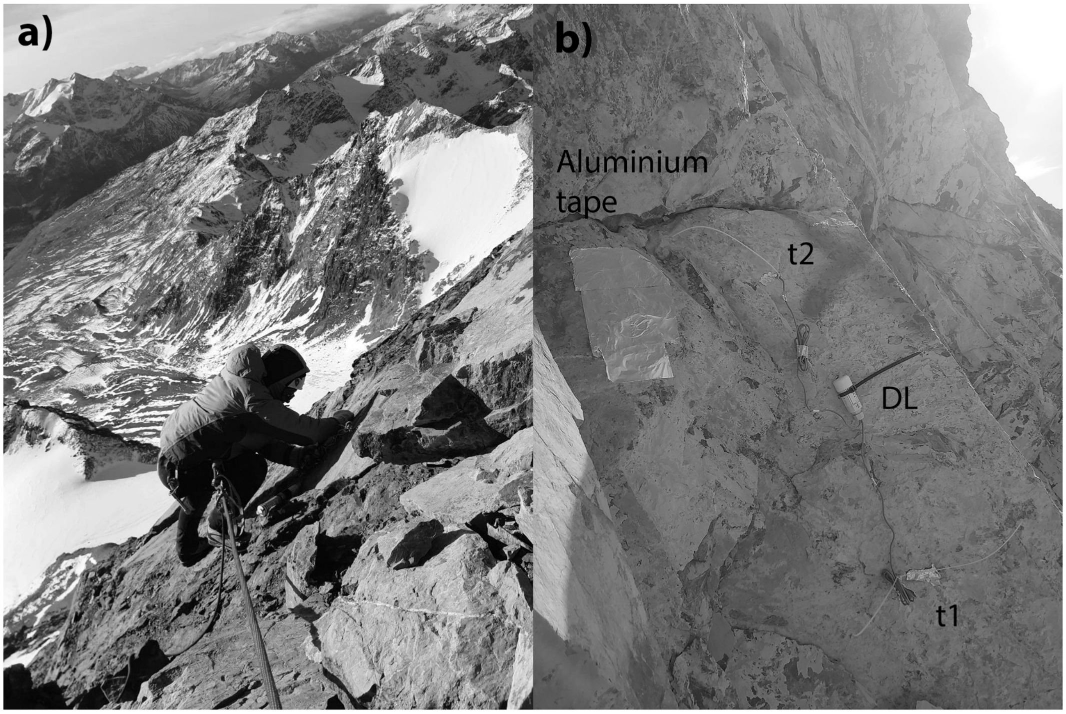

Fig. 2. a) Drilling at the location of Tb and b) disposition of the thermistors (t), datalogger (DL) and aluminum tape at Tb.

Table 2
Timings of the UAV surveys and number of images acquired in relation to the maximum and minimum RS energy input expressed as RSTs (°C) and solar radiation at the AWS (W m^{-2}).

Date	Time	Number of photos	Weather conditions around the summit	Surface temperature (°C) min (time) – max (time) at Te	Radiation (W m^{-2})
23/07/2021	08:45–09:00	333	Clear	3.5 (06:30) – 26.3 (16:00)	n.a.
23/07/2021	12:15–12:30	253	Clear		
13/09/2021	10:30–10:45	352	Partially cloudy	1.9 (08:00) – 15.0 (13:00)	0.6 (06:30) – 908 (11:00)
13/09/2021	13:45–14:00	429	Partially cloudy		
22/07/2022	09:15–09:35	547	Clear	5.9 (07:00) - 30.5 (14:00)	0.6 (05:30) – 1098.1 (14:00)
22/07/2022	12:10–12:20	323	Clear		
22/09/2022	06:30–06:45	337	Clear	−0.1 (09:00) – 0.3 (16:30)	0.6 (07:00) – 751 (13:30)
22/09/2022	14:45–15:00	341	Clear		

(MARST), the Thawing Degree Days (TDD) and Freezing Degree Days (FDD) (Molau and Mølgaard, 1996).

Using the Ta thermal daily gradient (GA) from 15 and 40 cm of depth, it has been possible to extrapolate ALT (as maximum depth of the 0 °C isotherm). GA was then used to extrapolate the ALT in Te from the maximum daily mean at 15 cm, assuming that this gradient can be considered constant throughout the rock wall due to the quite good homogeneity of the rock. In a same way, also the Ta GA from 2 and 40 cm of depth (GA2) was computed and used to extrapolate the ALT in Tc and Td from the maximum daily means at 2 cm. In addition, each site was equipped with a quadrat (20 × 20 cm) of aluminum tape to make the location recognizable from the aerial thermal images thank to its high reflection property (Grechi et al., 2021).

Air TDD (TDDa) and mean annual air temperature (MAAT) at the sites were calculated through a lapse-rate elevation gradient using 3 different closest AWSs ($R^2 > 0.99$) (Ponti et al., 2021a). The snow duration was obtained by counting the days with a smooth pattern of daily temperature variation (daily range < 0.5 °C) and the zero-curtain duration (Ponti and Guglielmin, 2021) by counting the days with daily variations between 0.2 and − 0.2 °C (accuracy of the thermistor).

3.3.2. Thermography and proposed model

The acquired thermal images (radiometric jpgs (RJPG)) were firstly converted into .TIFF files thank to the software ImageJ (https://imagej.nih.gov/ij/) and in particular its plugin ThermImageJ (https://github.com/gtatters/ThermImageJ). This procedure allowed to convert multiple.RJPG into.TIFF files with temperature values readable by Metashape and ArcGIS. Subsequently, the raw.TIFF images were imported in Agisoft Metashape 1.8 and displayed as stretched color temperatures through the tool Set Raster Transform. Here, the images were treated with a typical structure from motion workflow (Nesbit and Hugenholtz, 2019; Ponti et al., 2021c; Ponti and Guglielmin, 2021; Scaioni et al.,

2019) (without ground control points) operated on radiometric data (Grechi et al., 2021). Indeed, the bundle adjustment algorithm works well even with single-band images with stretched values and not RGB digital numbers (DN). The result was an unfiltered 3D thermal point cloud without georeferenced system, in fact.RJPG images cannot contain a geotag information (DJI communication). Therefore, geotagged RGB images from the best (good weather, high number of images and tie points and no shadows/snow) drone survey were also run in Metashape to obtain a georeferenced 3D RGB point cloud that was used as reference cloud. Indeed, all the thermal 3D point clouds were imported in CloudCompare 2.13 (www.cloudcompare.org) as .PLY files and then co-registered onto the georeferenced RGB cloud selecting at least 5 control points through the Iterative Closest Point (ICP) method (Maset et al., 2017). This process permitted to have a root mean square error (RMSE) of the alignment procedure and minimize the errors (Table 3).

Once registered, the best minimum common thermal point cloud (13/09/2021) was selected and the scalar values of the other thermal entities (temperatures) were assigned to it with the Scalar Field function (Guilbert et al., 2020). In this way, it was possible to calculate the temperature differences of different days on the same point cloud. Similarly, the RGB point cloud was converted in reflectance values according to Rippin et al. (2015). The assumption consists in a direct relationship between the signal recorded by the camera and the surface albedo or reflectance. This is justified because most of the energy reflected by many materials, including snow, is in the visible portion of the electromagnetic spectrum (Corripio, 2004). The digital numbers (DNs) of R, G and B bands of the point cloud were then summed and converted in reflectance (0–1) as proxy of the albedo at each point (Rippin et al., 2015). To strengthen the relation between image DN and albedo we validated through linear regression the relation with different color rock samples in the field with a portable camera and a portable pyranometer. With these data we were allowed to calculate the 3D spatial ATI ($°C^{-1}$) of the investigated days according to the formula:

$$ATI = (1 - A)\,\Delta T^{-1} \tag{1}$$

where A is the albedo and ΔT (°C) the surface temperature range for a selected day (Maltese et al., 2010).

In this study, due to the difficulties of assessing the rock properties (thermal conductivity, and specific heat), we decided to rely on the ATI as proxy of the real thermal inertia (Maltese et al., 2010; Minacapilli et al., 2012; Verstraeten et al., 2006). Thermal inertia and ATI depend on the porosity of the substrate that is here generally quite low (not far from here in the same lithology, porosity was measured to be always lower than 5 %, Guglielmin et al., 2018) and by the water and ice content that are more variable. We therefore averaged the ATI values calculated for the 3 different dates (13/09/2021, 22/07/2022, 22/09/2022).

Table 3
Photogrammetric characterization of the 3D point clouds obtained from the UAV surveys. The images reprojection error (px) was extracted from Agisoft Metashape 1.8. The root mean square error (RMSE, m) indicates the registration error of each point cloud on the one representing the 13/09/2021 at 13:30 survey (bold). The choice of this reference point cloud was based on the highest number of photos and less shadows on the RS. This thermal point cloud was previously registered upon the corresponding RGB.

Date	Number of points	Reprojection error (px)	CC RMSE (m)
23/07/2021 09:00	591,779	0.3–1.4	3.41
23/07/2021 12:30	1,173,035	0.2–0.8	1.73
13/09/2021 10:30	688,315	0.3–3.3	2.03
13/09/2021 13:30	696,238	0.2–1.0	2.07 (to RGB)
22/07/2022 09:00	802,735	0.2–0.9	2.59
22/07/2022 12:00	723,210	0.3–0.7	1.26
22/09/2022 06:30	1,098,693	0.4–1.1	3.58
22/09/2022 15:00	1,188,769	0.3–1.0	2.11

Because ATI itself is an indicator of the variability of the rock temperature (thus a thermal property of the rock), we decided to transform it into the heat transfer coefficient (HTC), that is the multiplication of ATI per a flux of incoming energy (Robertson, 1988) which better explains the transmission of the heat flux in depth. This passage firstly permits to solve the equation (HTC = ATI * heat flux) to have a correct unit of measure ($W\ m^{-2}\ °C^{-1}$). Secondly, the addition of an energy flux permits to have an indicator of the surface energy balance and its spatial variability on the rock wall. Therefore, we used the daily (at the date of the maximum thaw depth) potential solar radiation ($W\ m^{-2}$) obtained from the DEM in ArcGIS 10.8 as index of the different incoming heat flux for 2021 and 2022. In this way, ALT relates with HTC because it is the expression of the heat flux capability to reach inner rock layers (Fig. 3). Therefore, successively, we multiplied the 3D point clouds in CloudCompare to have a spatial distribution the HTC: the averaged ATI multiplied by the potential solar radiation at the different dates. Finally, we used a linear regression deriving from the observation points (thermistors) to transform the 2021 and 2022 HTCs into a continuous spatial distribution of ALTs.

The performance of the modelled ALT was conducted by R^2 and *p*-value, while the validation consisted of a 5-fold cross validation performed on randomly selected 3-sample test sets, of which we checked the R^2, p-value, mean absolute error (MAE) and root mean square error (RMSE) (Colombo et al., 2023; Kenner et al., 2019; Magnin et al., 2019).

3.3.3. ALT classical modelling

Our proposal of ALT calculation (spatially distributed) was compared with the Stefan's solution (Zhang et al., 2005), that permits to calculate ALT from the TDDa (la Cour Bohr et al., 2015), when the surface TDD are not known:

$$ALT = E \bullet \sqrt{(Nt \bullet PRI \bullet TDDa)} \tag{2}$$

where Nt are the N-factor of thaw (unitless), TDDa is the air degree-days of thaw (°C day), PRI is the potential radiation index (unitless) and E is the edaphic factor (Nelson and Outcalt, 1987):

$$E = \sqrt{((Kt \bullet S)/(Pb \bullet w \bullet L))} \tag{3}$$

where Kt is the thermal conductivity of the dolostone ($4.92\ W\ m^{-1}\ s^{-1}$) (Guglielmin et al., 2018) and assumed to be constant (Magnin et al., 2017), S is a scale factor ($86{,}400\ s\ day^{-1}$), Pb is the bulk density of the dolostone ($kg\ m^{-3}$), w is the water content of dolostone ($kg\ kg^{-1}$) and L is the latent heat of fusion ($333{,}660\ J\ kg^{-1}$) (Zhang et al., 2005).

With the average Nt obtained from the 4 thermistors (7.5), it is therefore possible to calculate a spatial distribution of the ALT from the TDDa. TDDa were indeed extrapolated throughout the rock wall using the linear regression lapse-rate equation of the 3 closest AWSs ($y = -1.2348\times + 4309.1$, $R^2 = 0.99$).

Moreover, also the surface TDD were used, not Nt-corrected, with the same formula, by assuming that the surface TDD relates with the elevation of the sites through a linear regression ($y = -1.1653x + 4808.7$, $R^2 = 0.83$).

The dolostone density and water content have been tested in laboratory after collecting surface (0–10 cm) samples (2 samples per site) from all the thermistors' sites. The averages are, respectively, 2312 kg m^{-3} and 0.0031 kg kg^{-1}.

4. Results

4.1. Temperature data

The RST inter-site differences are quite strong during the summer, while quite similar in winter. In the two summers available (although the 2021 is not complete) the RST is almost independent by the air

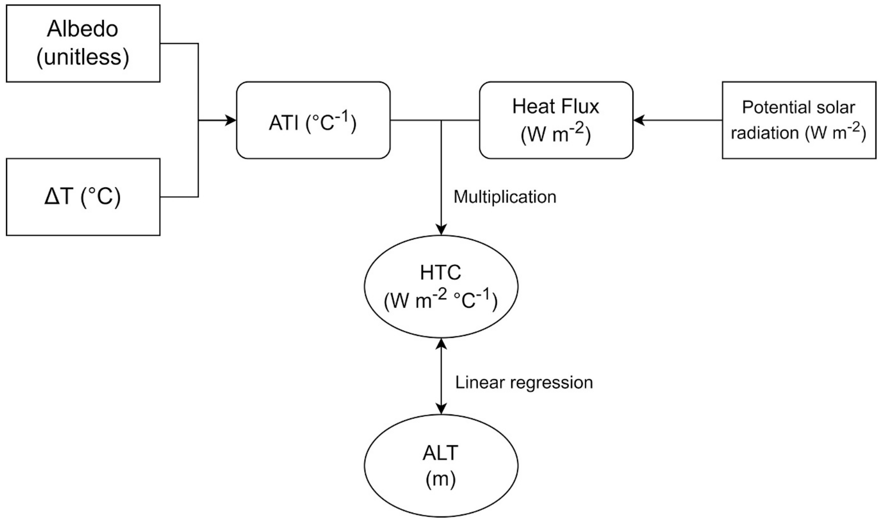

Fig. 3. Schematic representation that illustrates the association of the thermal parameters to yield the ALT.

temperature because some sites (Ta and Td in 2021 and Td also in 2022) exceeded 6 °C respect the maximum air temperature (9.7 °C on 14/08/21 and 10.2 °C on 20/7/2022) but the others (Tc and Te) showed RST lower or equal to the air temperature in 2021 and only 2–3 °C warmer than air temperature in 2022 (Fig. 4).

If we consider the mean annual RST (MARST) in the hydrological year (2021–22), it is quite variable, ranging between −2.8 °C in Te and +1.4 °C in Ta, as well as the TDD ranging between 524 (Te) and 1072 °C day (Ta) (Table 4). Despite the calculated MARST at the lowest elevation (Ta) and at the highest elevation (Te) was respectively the highest (+1.4 °C) and the lowest (−2.8 °C) MARST, the MARST did not follow an altitudinal trend like the MAAT. Indeed, Td, despite its higher elevation (3570 m a.s.l.), showed a warmer temperature (−0.4 °C) than Tc (−2.3 °C), located 100 m lower. MARSTs were warmer than MAATs of a minimum of 3.6 °C (Tc) and a maximum of 6.1 °C (Ta). The PRI indicated that Tc and Td absorbed more radiation than Ta and Te, as also observed from the potential incoming radiation at the ALT dates (2021 and 2022) that were maximum for Tc (6646.1 and 7315.8 W m^{-2}) and minimum for Ta (5347.0 and 5449.1 W m^{-2}). The snow days, independently from MARST, were maximum at Te (230) and minimum at Tc (83).

A variable zero-curtain period was observed, generally between the earliest 21/04/22 and the latest day 22/06/22. It ranged from 4 days (Tc) to a maximum of 38 days in Ta.

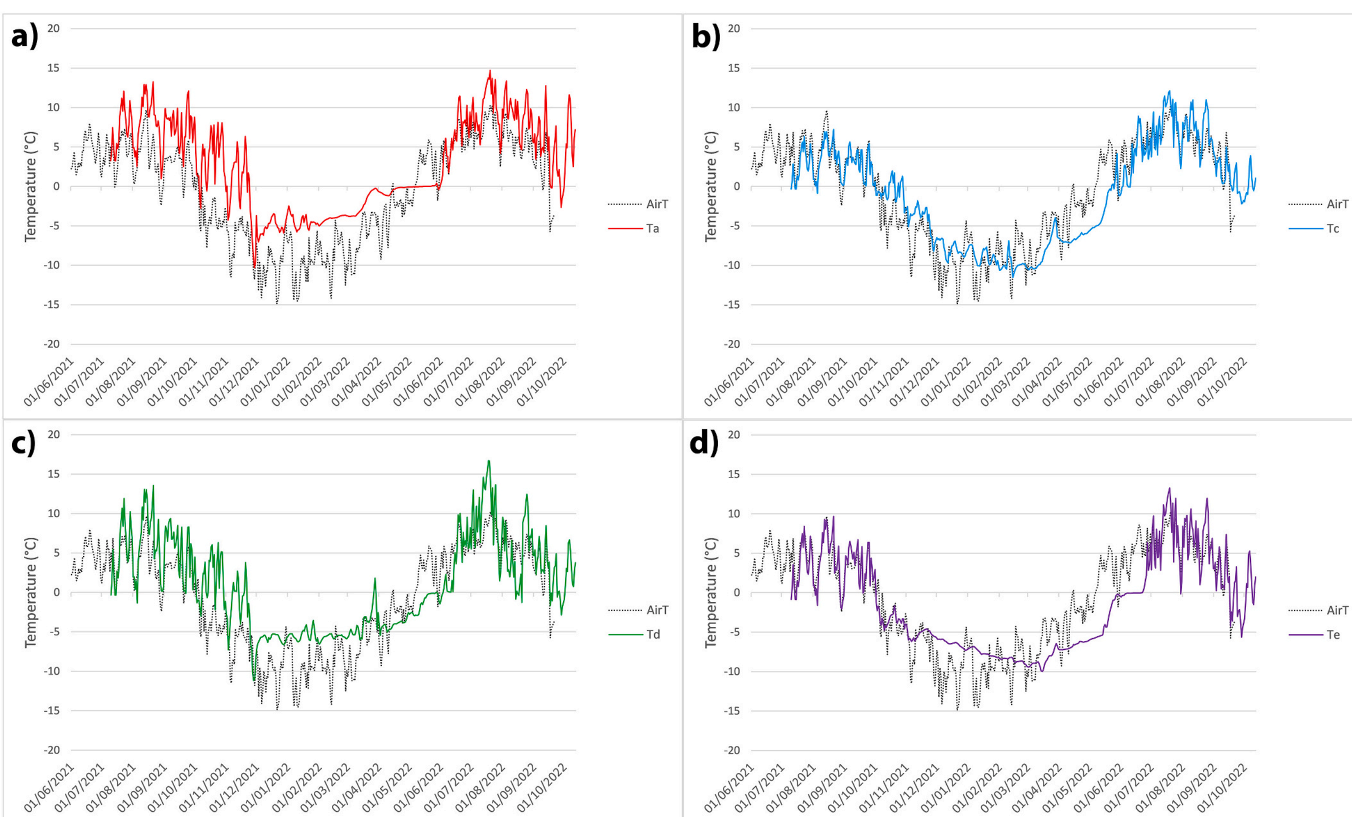

Fig. 4. Mean daily RSTs at the thermistors' sites compared with the mean daily air temperature at the AWS (3050 m a.s.l.). a) Ta, b) Tc, c) Td, d) Te.

Table 4
Thermal and topographical characterization of the sites calculated from both the thermistors data and the UAV flights.

	Unit	Ta	Tc	Td	Te
Albedo		0.55	0.64	0.51	0.63
MAAT at the thermistor	°C	−4.7	−5.9	−6.4	−6.8
MARST	°C	1.4	−2.3	−0.4	−2.8
TDD	°C day	1072.5	648.7	762.3	523.9
FDD	°C day	−569.8	−1499.5	−915.1	−1549.7
Zero-curtain	days	38.0	4.0	10.0	18.0
PRI		1.0	1.2	1.2	1.1
Potential radiation 21/08/21	W m^{-2}	5347.0	6646.1	6417.3	5898.9
Potential radiation 20/07/22	W m^{-2}	5449.1	7315.8	6937.4	6230.3
ALT date 2021		21/08/2021	21/08/2021	21/08/2021	25/09/2021
ALT 2021	cm	221.6	121.5	226.6	107.9
RST range 13/09/21	°C	13.03	21.33	16.01	14.39
ATI 13/09/21	°C^{-1}	0.0142	0.0103	0.0167	0.0135
ALT date 2022		20/07/2022	19/07/2022	18/07/2022	19/07/2022
ALT 2022	cm	204.1	171.1	234.9	187.3
RST range 22/07/22	°C	13.3	20.4	16.8	12.1
ATI 22/07/22	°C^{-1}	0.0343	0.0245	0.0269	0.0291
RST range 22/09/22	°C	26.0	36.6	25.9	21.9
ATI 22/09/22	°C^{-1}	0.0304	0.0184	0.0242	0.0258

As a consequence of a warmer and anticipated summer in 2022, the ALT (among the sites) occurred between 18 and 20/07/2022, while in 2021 occurred between 21/08 and 25/09/2021. In 2021, ALT ranged between 121.5 cm in Tc and 226.6 cm in Td, while in 2022 between 171.1 (Tc) and 234.9 (Td). Because of the warmer summer, ALT was averagely greater in 2022 than 2021 (+45.8 cm) with the largest variation in Te (+79.5 cm), except in Ta where it was reduced of 17.5 cm.

4.2. Thermal data by thermography

From the RGB 3D model, the average albedo was extracted at each site, ranging from 0.51 (Td) to 0.64 (Tc), a plausible range for dolostone (Galvao and Vitorello, 1995).

The remotely sensed daily surface temperature range was highly dependent on the timing of acquisition, however, for each acquisition, the highest values were in Tc (from 20.4 to 36.6 °C), while the lowest in Ta in 2021 (13.03 °C) and in Te in 2022 (12.1–21.9 °C). Due to this variability and the variation of albedo, the ATI changed both in space and time. However, a similar pattern was obtained for the 2 dates in 2022, which showed the minima in Tc (0.0245 and 0.0184 °C^{-1}) and the maxima in Ta (0.0343 and 0.0304 °C^{-1}), while in 2021 the maximum was obtained in Td (0.0167 °C^{-1}) and the minimum in Tc (0.0103 °C^{-1}). Averagely, ATI was lower of 0.013 °C^{-1} in 2021 than 2022 (Table 4).

A more detailed pattern of the ATI spatio-temporal variation is visible in Fig. 5. Here, it is clear that ATI on the 22/07/2022 is always greater than on the 22/09/2022 and 13/09/2021. By looking at the averages, it is possible to see that Ta had the greatest ATI (0.0263 °C^{-1}), followed by Te (0.0228 °C^{-1}), Td (0.0226 °C^{-1}) and Tc (0.0177 °C^{-1}).

In Fig. 6 it is possible to see some examples of the spatial distribution of the parameters used to calculate the ATI and the HTC. The calculated albedo showed values ranging between 0.03 and 0.99 with a median value of 0.59. The lowest albedo was located at the mid-elevate part of the rock wall where darker dolostone is present (averagely 0.3), whereas the higher albedo at the top or bottom part where light dolostone and debris (scree slopes) are present (averagely 0.65). The cumulative solar radiation pattern of 22/07/2022 showed values ranging between

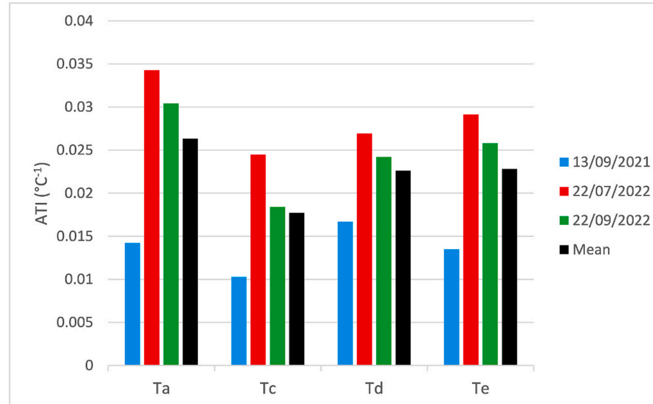

Fig. 5. ATIs (°C^{-1}) extracted from the UAV flights (both RGB and thermal) at the thermistors' sites for all the dates in which the surveys were conducted.

2500.0 and 7787.6 W m^{-2}, with an average of 6295.0. The highest frequency radiation accounted for 6700–7000 W m^{-2} and was related to the DEM, specifically to the slope and aspect of the rock wall. Indeed, very steep or shadow areas registered the lowest solar radiation, such as the mid to bottom-mid elevation part. The maximum difference of RST recorded on the 22/09/2022 showed a very different pattern from the albedo and solar radiation. The minimum temperature range was 10.0 °C, while the maximum 44.0 °C, with an average of 25.3 °C. The most frequent difference of temperatures ranged between 23.6 and 25.8 °C. It is observable that the highest ranges were recorded at the lowest part of the rock wall, where some rock debris is present, while the smallest at the troughs where shadows last for almost the entire day. The average ATI depended on the albedo and the single-day RST differences and ranged between 0.0 and 0.05 °C^{-1}, with an average of 0.026 °C^{-1}. The most frequent values set between 0.02 and 0.023 °C^{-1}, with the lowest values at the bottom (debris) and top-western sector (light dolostone), while the highest at central (shadow and darker dolostone) and top part (relatively dark dolostone) of the rock wall. This showed an opposite pattern respect to the albedo that it is due to the ATI formula.

We found that, grouping 2021 and 2022 observations (total of 8 cases), ALT well related with the HTC. We excluded 3 random observations from the dataset (Ta,e for 2021 and 2022) in order to have the 1st-fold calibration (5 observations) and validation (3 observations) sets and define the chosen model. The linear regression between ALT and HTC showed a good calibration ($R^2 = 0.9$, $p < 0.02$) of the model with the equation expressed in Fig. 7. The cross validation of the model showed an average R^2 of 0.97 with an average RMSE and MAE of 18.5 and 15.3 cm, respectively (data shown in Section 5.1).

Fig. 8 shows the spatially distributed products HTC for 2022 and modelled ALTs for the years 2021 and 2022 by using the equation showed in Fig. 7. The HTC for 2022, that is the product of the mean inter-annual ATI and the cumulative potential solar radiation at the ALT date, ranged between 35 and 300 W m^{-2} °C^{-1} with an average value of 148.8 W m^{-2} °C^{-1} (median of 138.5) and the highest number of points (>95 %) ranged between 120 and 140 W m^{-2} °C^{-1}. Only the <1 % of the points was <69 W m^{-2} °C^{-1}, while the >99 % was >269.9 W m^{-2} °C^{-1}. It is important to notice that a similar pattern of ATI is showed, with the lowest values in correspondence of the bottom (debris) and top-western sector (light dolostone), while the highest at the top part (relatively dark dolostone). Differently from ATI, the central part is dominated by mid values, whereas the top part is characterized by both low and high intensities. A similar pattern is maintained in the ALT distribution after the application of the linear regression model. Indeed, the regression produced ALT values with an average of 198.7 cm (median of 179.7) and the (>95 %) ranging between 125 and 175 cm in 2021, while with an average of 228.0 cm (median of 200.0) and (>95 %) ranging between 150 and 200 cm in 2022.

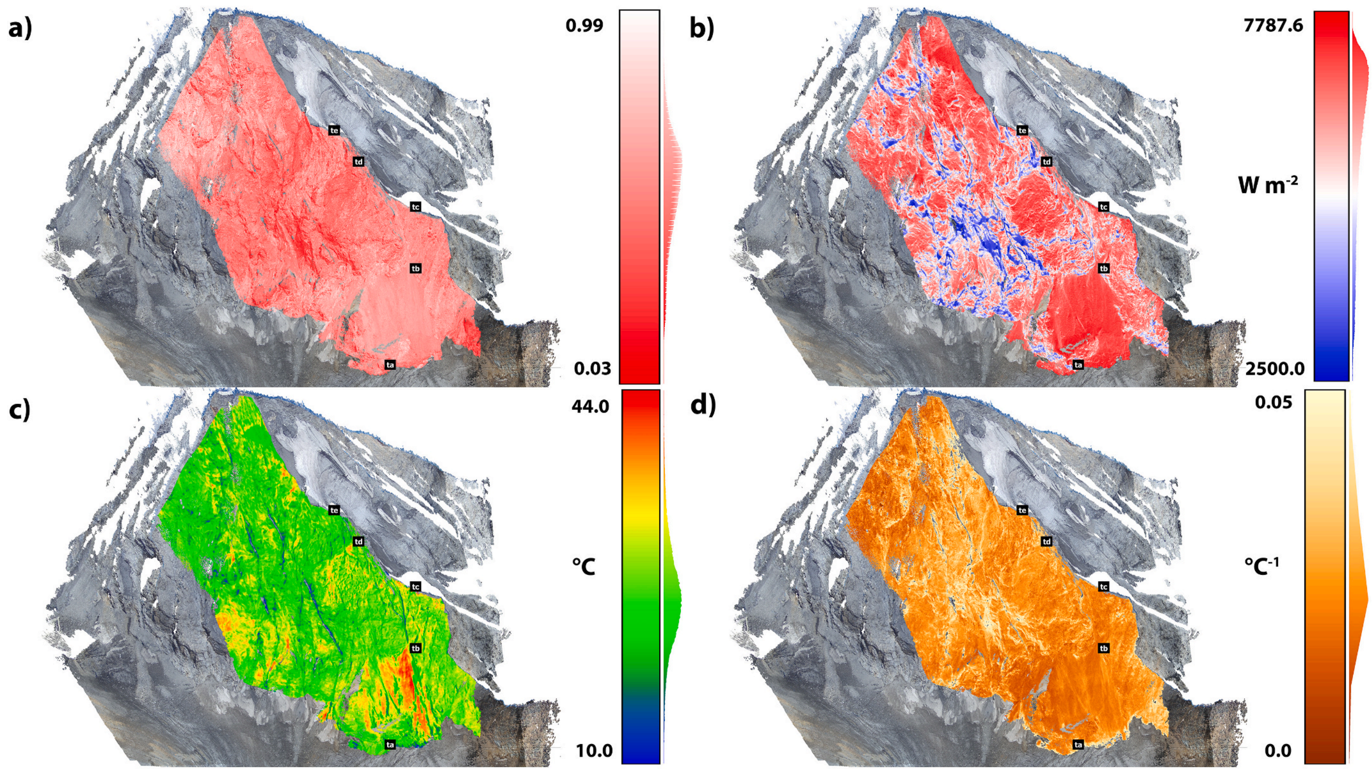

Fig. 6. 3D models of the parameters that have been used for the calculation of the HTC. a) Albedo, b) potential solar radiation on 22/07/22, c) RST range on 22/09/22, d) 2021–2022 average ATI. Please note that the stretched color scale sets between the minimum and maximum values and a relative frequency of the values lays at the right part of it.

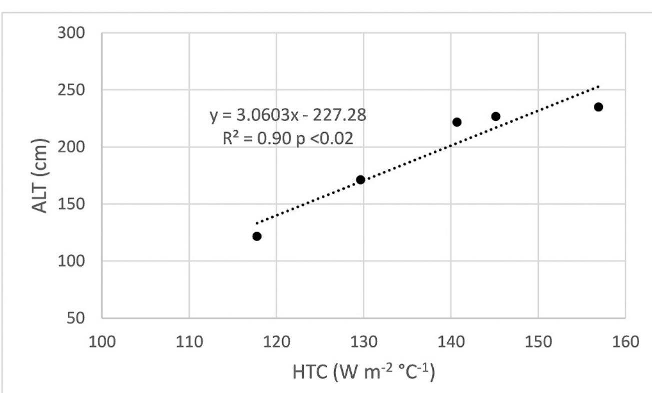

Fig. 7. Linear regression between 2021 and 2022 ALTs and corresponding HTCs at the thermistors' sites. These random 5 observations on the total of 8 have been used for the calibration of the model. The remaining 3 observations were used for one of the 5-fold cross validations in one other linear regression (see Section 5.1).

Differently from what expected, the ALT did not follow an altitudinal trend, rather, both very high and low thicknesses were found at high and low elevations. Except for the bottom-eastern border, the whole top part is constituted of a high spatial variation, apparently dominated by a horizontal gradient that leads low values from West to high values at East, getting closer to the top glacier. Oppositely, this gradient is not visible at the central or bottom part, where values remain relatively mid or low, respectively. However, the same high thicknesses were present at the bottom border next to the Eastern Gran Zebrù glacier. Snow patches were persistent at the bottom-western limit of the rock wall and here values reduced, despite the presence of the glacier body below the snow and debris.

The comparison between ALT 2021 and 2022 shows that, at a first glance, the areas with the maximum thickness remained the same, however, what really incremented is the green class, indicating an increase from 0–200 cm to 200–400 cm, especially in the central and the bottom-right parts (Fig. 8).

Concerning ALT change between 2021 and 2022, the highest number of points (>95 %) lays between 25 and 35 cm of ALT increase both on rock and debris and the mean value is 29.3 cm (median of 27.7). Higher values (>50 cm, up to 200 cm) are found at the mid-elevation eastern sector, where the shape of the rock wall starts to change aspect (towards East), or at the top-eastern part, where the contact with the glacier is closer. The same happens at the contact with the bottom glacier, similarly to the maximum ALT of 2022. Surprisingly, some areas showed a decrease of ALT, up to −90 cm, both at low and high elevations, but mainly at the western part of the rock wall. Moreover, from the 3D view, the lowest values correspond to the steepest part of the rock wall that will be treated in the discussion. It is also interesting to notice that the areas subjected to a decrease of ALT were areas with a thinner ALT (0–200 cm), whereas the areas with thick ALT (>600 cm) underwent a considerable increase (>100 cm) (Fig. 9).

4.3. Comparison with other models

There are two possible ways to model the ALT with the Stefan's equation: either to use the ground surface TDD (Hrbáček et al., 2020) or the TDDa corrected with the N-factor (Zhang et al., 2005). The average N-factor among the sites resulted to be 7.5 and it was used to convert the TDDa into TDD at the rock surface (RS TDD) along the rock wall. Above 3490 m a.s.l. the TDDa are absent all year long and, therefore, according to the Stefan's equation that used the TDDa, the ALT is 0 and permafrost is on the surface (Fig. 10c). In this way we obtained an ALT ranging from 0.71 to 207.4 cm with an average of 131.8 cm and permafrost at the rock surface above 3490 m a.s.l. Conversely, the RS TDD were all positive and

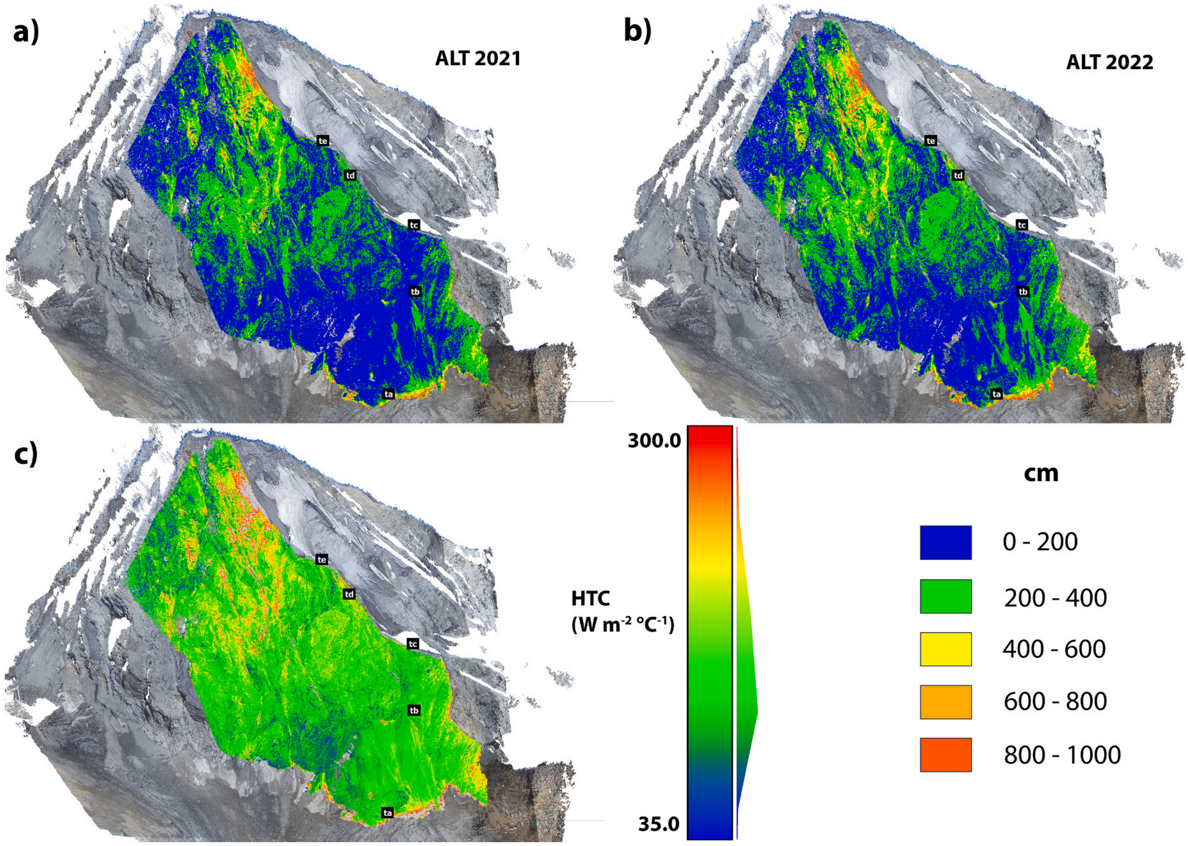

Fig. 8. 3D spatial distribution of the modelled ALT in 2021 (a), 2022 (b) and the calculated HTC in 2022 (c). Please note that the stretched color scale of HTC sets between the minimum and maximum values and a relative frequency of the values lays at the right part of it. Conversely, the color classes at the bottom-right of the figure shares the same classes for ALT in 2021 and 2022.

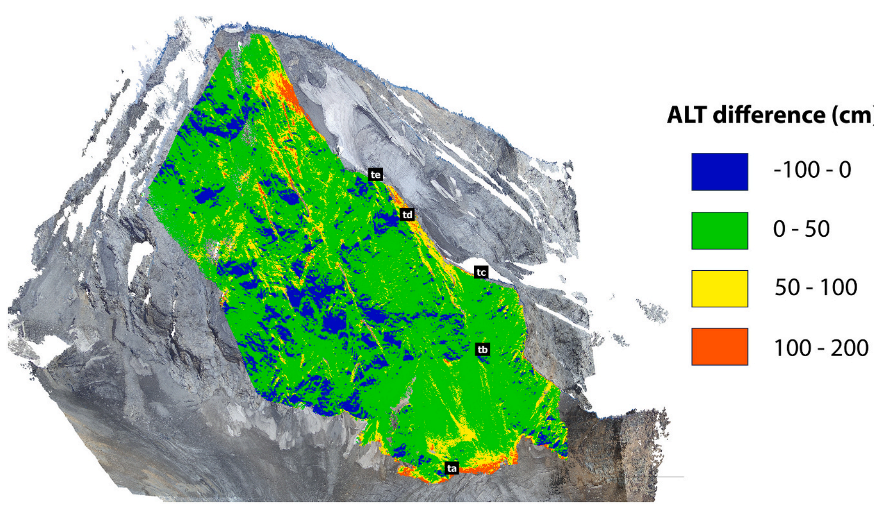

Fig. 9. 3D spatial distribution of the ALT difference from 2021 to 2022.

this indicated a theoretical discrepancy between the two approaches. As a result of the RS TDD application, the ALT along the rock wall ranged between 11.5 and 205.3 cm with an average of 163.7 cm (Fig. 10b). An altitudinal gradient is barely visible, but also dominated by the effect of the PRI. In general, the Stefan's ALT resulted to be almost one order of magnitude smaller than the thermal model (Fig. 10a). Moreover, this different result masked the previously described horizontal gradient and the variability at the snow and glacier borders (Fig. 8). However, below 3490 m a.s.l., a wider range of Stefan's TDDa ALT is present compared to the RS TDD ALT. For TDDa the altitudinal pattern is more evident than RS TDD, but both show a slight increase of thickness at the bottom glacier border, similarly to what proposed in our model. In order to evaluate the relation between the ALT and the permafrost presence, the APIM (Boeckli et al., 2012) shows a likely presence of permafrost at the central western sector, where the proposed model shows both high and low ALT values (Fig. 10d). More interestingly, the stripe-shaped area of permafrost “in nearly all conditions” maintains a certain distance from the 2 glaciers, almost indicating that the presence of a glacial body

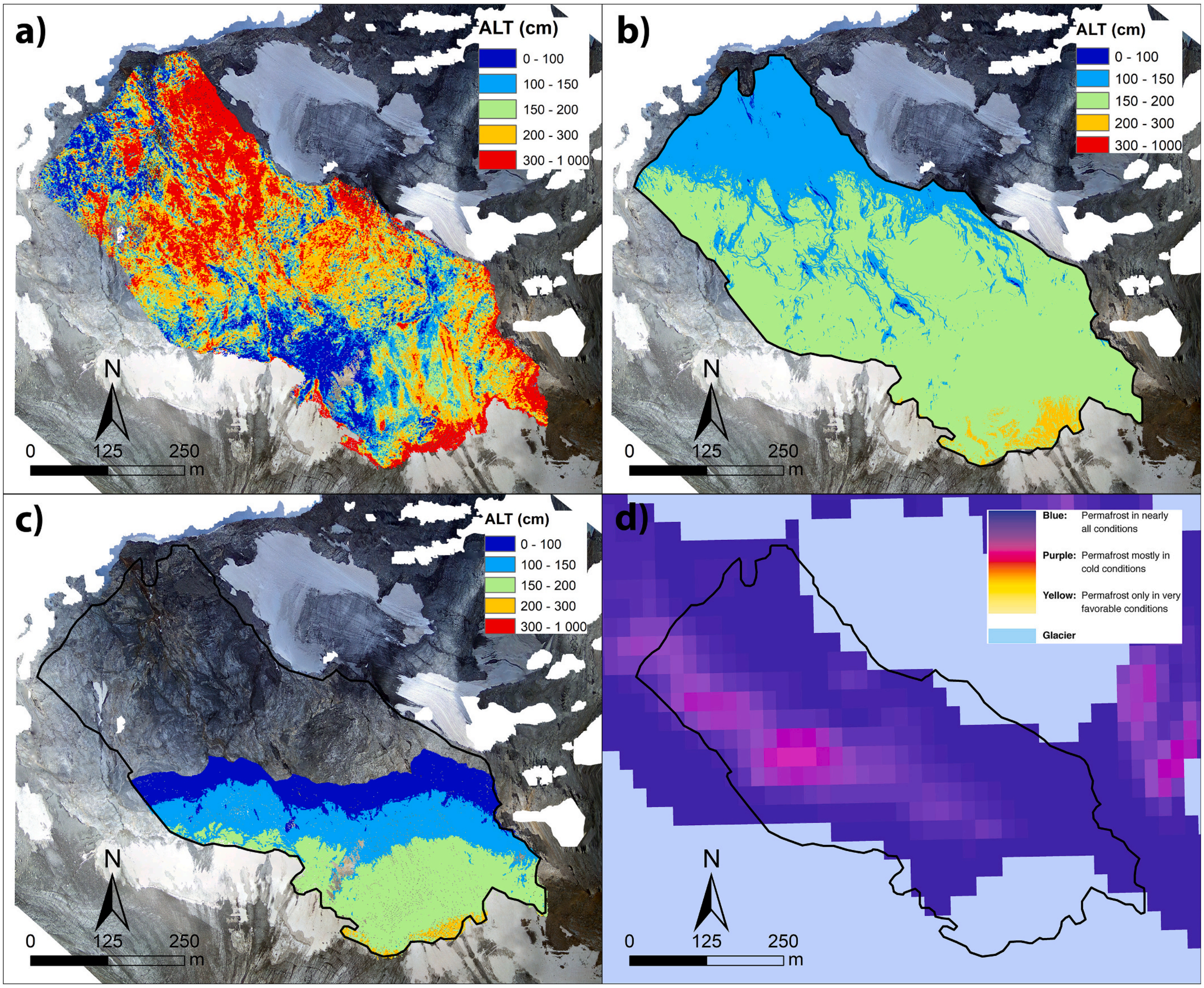

Fig. 10. 2D comparison of the ALT for our proposed thermal model (a) and ALT obtained through the Stefan's equation with RS TDD (b), air TDD (c). (d) Instead shows the probability of permafrost occurrence according to APIM.

disfavors the formation of permafrost. However, this pattern is not visible, at least, in the modelled ALT (Fig. 10a). Indeed, one would expect shallower ALTs throughout the most probable permafrost conditions.

5. Discussion

5.1. *Uncertainties and assumptions*

The major assumptions of the proposed model lays on the thermistors thermal gradient used to assess the in situ ALT. Beside the fact that we used different gradients per site (see Section 3.3.1), we also rely on the gradients found in other studies. For instance, Magnin et al. (2015b) found that boreholes at similar elevation but different aspects had not big difference of thermal gradients within the first 2 m of depth. Likewise, Nigrelli et al. (2022) found that the thermal gradient between 30 and 50 cm did not significantly vary at different aspects and same slopes. This could mean that elevation, slope and aspect substantially affect the source of the heat flux (surface temperature) and less likely the inner thermal gradient for the same lithology. Moreover, the small amount of water content (ranging between 0.0015 and 0.006 kg kg^{-1}), rock density (ranging between 2.10 and 2.46 kg m^{-3}) and rock porosity (ranging between 0.06 and 0.67 %) that we obtained at each site could not affect the thermal gradient significantly. At the same way, due to the homogeneity of the rock surface (no big fractures) at the sites, the lateral heat flux can be negligible, differently from Magnin et al. (2015b) and Rico et al. (2021).

Other studies placed a similar number of thermistors (3 to 5) (Nigrelli et al., 2022; Rico et al., 2021; Hipp et al., 2014), even though they were located at different aspects (NW to SE) (Hipp et al., 2014). Here, we focused on the representation of a South-exposed rock wall with the thermistors' aspect ranging from SE to SW, similarly to Rico et al. (2021) (4 thermistors N to NE).

Concerning the thermistors' measurements, the manufacturer (Onset) declares an accuracy of 0.2 °C from 0 to 50 °C and 0.25 °C from −40 to 0 °C. These specifications are in line with other works which calibrated iButtons (accuracy of 0.5 °C) down to an accuracy of 0.25 °C (e.g. Draebing et al., 2017).

Since the thermal images did not contain the position information (geotag), differently from the RGB images, we had to register the thermal onto the RGB point clouds. We therefore obtained a range of RMSE of 2.07–3.58 m that is negligible because we did not rely on an absolute coordinate system and, more importantly, this range is undetectable considering the whole dimensions of the investigated rock wall.

Moreover, the registration errors could not affect the values extracted from the clouds in correspondence of the thermistors since an average of surrounding pixels was picked.

Another assumption consists in the albedo calculation of the rock wall. The obtained range (0.03–0.99) does not fit the naturality of landscapes, but it is more likely that single pixels' high (total) reflectivity or complete shadow might have caused such extremes, although they did not compromise the final ALT result. Indeed, the pixels frequency distribution showed that the extreme albedo values >0.8 and <0.2 had a very low frequency (1 % each).

Another weakness of the proposed model lays on the fact that we used the potential solar radiation at the date of the maximum thaw depth (AL). It is improbable that a single-day heat flux caused such thaw depth but rather it is a seasonal effect of the surface energy balances. However, we wanted to rely on an easily accessible parameter that resumed the topographic characteristics of the rock wall and kept the model reproducible (Kenner et al., 2019; Magnin et al., 2019; Hipp et al., 2014).

The totality of observations of our model consisted of 8 samples that we split up into 5 random couples of training sets (5 samples) and test sets (3 samples) to be able to calculate the R^2 for the test sets, that is a stronger solution than having 1-sample test sets (Kenner et al., 2019; Magnin et al., 2019). The chosen model (one of the training sets' linear regressions) had the most similar equation coefficients (m and q) to the linear regression model of the whole dataset but higher R^2 (Table 5). Moreover, the average RMSE and MAE indicated errors that are in line to other research studies (Zhang et al., 2021; Qin et al., 2017) and representing less than the 10 % of the average ALT, even though the *p*-values were not all significant due to the reduced dataset (Table 5) but never treated elsewhere (Colombo et al., 2023; Kenner et al., 2019; Magnin et al., 2019).

5.2. ALT modelling and comparison

In this study thermal inertia and potential solar radiation are the most important parameters affecting ALT. Even though the effect of solar radiation is well demonstrated (e.g. Guglielmin and Cannone, 2012), it is the first time that thermal inertia is applied to monitor the characteristics of permafrost (ALT). Little was done to map permafrost using this property. The only research was conducted upon Mars (Bandfield and Feldman, 2008; Paige, 1992; Paige and Keegan, 1994). The results we obtained agree with the northern hemisphere of Mars at low latitudes, where high surface thermal inertia (or HTC) and lower albedo were associated to greater permafrost depths, thus thicker AL (Bandfield and Feldman, 2008; Putzig et al., 2005). On the rock wall, the high values of HTC associated with greater ALT can be explained by the energy transfer: a higher surface thermal inertia means that the rock surface is minorly affected by the above thermal fluctuations and therefore the absorbed energy is conducted into the deeper layers fastly. Conversely, if the thermal inertia is low, it means that all the above energy flux is converted into temperature fluctuations of the surface and the heat transmission cannot reach deeper layers easily (Bandfield and Feldman, 2008).

Our results demonstrate that the entire Gran Zebrù South face is in permafrost condition. Indeed, maximum ALTs in the Alps have been recorded to reach 10 (Magnin et al., 2015a), 12.1 (PERMOS, 2022) and up to 15 m (Draebing et al., 2017; Draebing et al., 2014). If we consider similar locations on the Alps, it is possible to notice that the ALT in bedrocks for a recent period (2011−2022) ranges between 3.6 and 10.4 m, thus comparable with our results (between 0 and 10 m) (Table 6). Such few extreme values were reached due to low radiation zones caused by permanently shadow conditions (fractures) (Magnin et al., 2015a) or high potential radiation towards the top of the summit, never being shadowed by the peak topographic profile.

It is also important to underline that other simple models (Stefan's solution) can be applicable in alpine/mountainous areas (Bonnaventure and Lamoureux, 2013; Riseborough et al., 2008), but the choice of air/surface temperatures could change the results drastically (Fig. 10). Both TDDa and surface TDD underestimated the ALT and especially the TDDa provided permanently frozen surfaces that are not possible without a permanent snow/glacier cover. The use of air temperatures for ALT and permafrost modelling should be considered carefully (Bonnaventure and Lamoureux, 2013). Confirming this issue, for instance, in Antarctica it has been demonstrated that no evident air warming trends led to ALT thickening in any case (e.g. Guglielmin and Cannone, 2012).

The best available permafrost model for the Alps (APIM) (Boeckli et al., 2012) helps giving an idea of the permafrost occurrence in the Alps and it is a useful mean of comparison (Magnin et al., 2015a), even though it is dated (Ponti et al., 2021a) and, in this spatial context, it is too coarse to represent the local scale variability (Etzelmüller, 2013). Therefore, relying on UAV permits to increase the resolution even better than the minimum metric resolution required (Magnin, 2015).

Here, we found a complex variability of ALT values close to the glaciers limits differently from what the APIM (Boeckli et al., 2012) and Magnin et al. (2015a) generally found. Indeed, while the first model shows low probability of permafrost close to the glaciers' limits, the second forecasts the opposite. In our case, a variety of values along the glacier limits could simply reflect the recently exposed subglacial topography (aspect and slope).

We also agree with the fact that MAGST (MARST) is not a good indicator of permafrost occurrence (Magnin et al., 2015b) since at 3230 m a.s.l. (Ta) a positive annual average and also an ALT of 204.1 cm (2022) (that is not the maximum modelled in the study area) were obtained. This decoupling effect could be related to the fact that very local favorable conditions are maintained in depth by fractures (Hasler et al., 2011; Magnin et al., 2019). Moreover, we found a distribution pattern of both MARST and ALT that did not follow an elevation trend, oppositely to Rico et al. (2021) and Magnin et al. (2015a). Indeed, Td MARST was considerably warmer than Tc (+1.9 °C) and ALT spatial distribution varied more horizontally than vertically. It is well demonstrated that the topography of summits can explain the distribution of surface temperatures and heat fluxes especially on sharp crests (Magnin et al., 2015a) turning into an ALT variability (Magnin et al., 2015b) that does not follow the elevation. Keeping in mind that not only elevation but also aspect and slope are very important for permafrost distribution (Draebing et al., 2022; Myhra et al., 2017), Table 7 wants to clarify the topographic relationship with ALT. Except of local decreases of ALT probably due to air ventilation in fractures (Hasler et al., 2011; Magnin

Table 5
Details of the proposed linear regression model with the equation's coefficients and the statistical parameters of each k_{th}-fold of the cross validation.

	K_{th}-fold	m	q	R^2	p	RMSE (cm)	MAE (cm)
Whole dataset model		3.2951	−272.9	0.64	<0.02		
Selected model (training set, 5 samples)		3.0603	−227.28	0.9	<0.02		
Test sets (3 samples)	1-fold			0.99	0.02	36.5	25.0
	2-fold			0.98	0.07	15.8	15.3
	3-fold			0.96	0.12	12.0	9.9
	4-fold			0.98	0.09	14.2	13.1
	5-fold			0.95	0.14	15.7	13.3
	Cross validation Mean			0.97	0.09	18.8	15.3

Table 6
Comparison of ALTs on bedrock sites in the Alps for a recent period 2011–2022.

Location in the Alps	Mean elevation (m a.s.l.)	Substrate	Year	Aspect	Lithology	ALT (m)	Reference
Schilthorn	3000	Bedrock	2018	Flat	Micaceous shales	10.4	PERMOS, 2022
Stelvio	3000	Bedrock	2018	Flat	Dolostone	3.76	Etzelmüller et al., 2020
Stockhorn	3379	Bedrock	2018	Gently South	Albite–muscovite schists	4.8	PERMOS, 2022
Mont Blanc Massif	3753	Bedrock	2011	South, 55° slope	Porphyritic granite	5.9	Magnin et al., 2015b
Cime Bianche	3100	Bedrock	2012	Slightly westward	Garnetiferous micaschists and calcschists	3.6–5.4	Pogliotti et al., 2015
Gran Zebrù	3512	Bedrock	2022	South, 46° slope	Dolostone	2.3 (average)	This study

Table 7
Spatial distribution of the ALT in 2022 and the ALT change between 2021 and 2022 according to the classified aspects and slopes occurring at the rock wall.

		Class	Frequency (%)	Mean (cm)	STD (cm)
ALT 2022	Aspect	N	0.1	225.0	353.9
		E	9.6	325.9	450.2
		S	83.3	229.4	160.2
		W	7.0	173.6	130.9
	Slope	0–18	0.9	391.5	338.5
		18–41	33.2	257.7	199.0
		41–60	52.9	227.8	221.6
		60–90	13.0	193.7	135.9
ALT Change	Aspect	N	0.1	112.4	107.4
		E	9.6	69.5	92.3
		S	83.3	28.6	24.9
		W	7.0	39.1	23.9
	Slope	0–18	0.9	91.0	55.4
		18–41	33.2	46.3	28.4
		41–60	52.9	29.7	41.5
		60–90	13.0	11.1	36.7

et al., 2015b; Rico et al., 2021), it is highlighted how there is no a clear trend with aspect showing maximum ALT at East and minimum at West probably because of the local weather conditions. Indeed, the Italian Alps are generally characterized by mornings with clearer sky compared to afternoons with greater atmospheric instability (Gladich et al., 2011) that hinders the solar radiation. Conversely, a good trend is obtained with the slope, indicating that steeper surfaces allow thinner ALTs as already demonstrated (Magnin et al., 2015a; Magnin et al., 2015b). The same trend is maintained also for the ALT inter-annual change with slope rather than the aspect. The majority of the rock wall facing South (83.3 %) underwent the smallest average AL thickening (28.6 cm) likely due to the different steepness that interested common aspects. Indeed, the majority of the rock wall with slopes of 41–60° (52.9 %) underwent a little warming (29.7 cm), smaller than gentler sectors and greater than the steepest. This is strictly related to the snow persistence on slopes (Draebing et al., 2017; Guglielmin et al., 2003; Magnin et al., 2015b; Magnin et al., 2019). Since our data rely on a totally snow free rock wall in both the summers, we can claim that winter snow accumulation can highly affect and determine the spatio-temporal variation of ALT (Draebing et al., 2017; Magnin et al., 2015b; Pogliotti et al., 2015), even in adjacent years. Probably, during the 2021–2022 winter, gentle slopes accumulated a thicker snow pack that buffered the low air temperatures resulting in a thicker AL in 2022 (Draebing et al., 2017; Myhra et al., 2017).

5.3. Trend and future risks

ALT increase from 2021 to 2022 averagely accounted for 29.3 cm with maximum values up to 200 cm. Apart from localized areas which underwent thinning due to very steep rock facades with a little winter snow accumulation (Draebing et al., 2017; Magnin et al., 2015b; Magnin et al., 2019; Pogliotti et al., 2015) or long snow persistence in fractures, the general trend of AL thickening is remarkable. Such a big average increase in a short time is not common on the Alps and not even elsewhere (Etzelmüller et al., 2020).

For the future scenario, at constant topography and assuming no wind drift snow, if the winter snowfalls will decrease in future (Kotlarski et al., 2023; Marty et al., 2017), we could possibly face a reduction of the ALT and then permafrost formation (Smith et al., 2022; Zhang, 2005). On the other hand, the anticipation of the maximum thawing date is widespread in the Alps (PERMOS, 2022) and we confirm it here (reaching one month). This can counteract the cooling gained during the winter (Magnin et al., 2015b). The overall AL thickening occurred mostly on gentle slopes (Table 7) that were able to accumulate thicker snowpack (Draebing et al., 2017; Magnin et al., 2015b; Pogliotti et al., 2015).

Here a good linear regression (ALTchange = −1.1896*slope + 85.525, $R^2 = 0.46$, $p < 0.001$) between ALT change and the steepness suggests how the steepest rock wall sectors meet little increase of ALT probably due to the small variation of snow cover (that cannot be accumulated due to the steepness). This fact, coupled with the reduction of winter snowfalls (Kotlarski et al., 2023; Marty et al., 2017) will cause a stronger thickening on the gentler slopes that is an ALT change increase of 1.18 cm degree^{-1} from 90° to 0°. This topic has a particular value in relation to the evolution of alpine ridges. Indeed, glacial valley and ridge profiles weathering trend will affect the mountain slopes through rock mass wasting (Augustinus, 1995), for instance steepening the mountain ridges (Delaloye, 2008; Evans and Clague, 1994; Galibert, 1960). If AL thickening produces large rock mass wasting (Legay et al., 2021; Ravanel et al., 2017), which in turn affects and steepens the ridges, this would be treated as a negative feedback of climate change on alpine permafrost, reaching an equilibrium and permafrost formation sooner or later. Similarly, the glaciers shrinking (thinning) future trend (Sommer et al., 2020) would expose quasi-vertical fresh rock walls which will favor the AL thinning, thus permafrost formation and stabilization of the rock (Wegmann et al., 1998) through a negative feedback. Conversely, the total disappearance of glaciers will create gentle slopes at the ex-glacier bottom and thus sufficiently great winter snow pack accumulation able to increase the ALT. However, these speculations could be founded depending on the spatio-temporal redistribution of the snow on the slopes (Draebing et al., 2017; Myhra et al., 2017; Pogliotti et al., 2015) and on the duration of the summer warming (snow-free period). Assuming as future trend a decrease of winter precipitation on the Alps (Kotlarski et al., 2023; Marty et al., 2017) and steepening of south-faced slopes as consequence of air warming (Zwieback, 2021), mountainous areas will definitely undergo changes that will be related both to the formation and degradation of permafrost with complex interactions (Draebing et al., 2022, 2017).

Independently from the AL thickening or thinning, the air temperature future change (both positive and negative) will affect the rockfall activity (Paranunzio et al., 2016). Therefore, in future research, it will be fundamental to track and map the weakness points along the rock walls like fractures with remote sensing techniques (Grechi et al., 2021; Mineo et al., 2022) and provide prediction models. The ALT change, depending on the exposed topography, will be coupled with the glacier shrinking in a complex mechanism that will provide destabilization of rock walls (Ravanel et al., 2017, 2013; Wegmann et al., 1998) and potential hazards. Despite a permafrost encroachment after the glacier thinning or verticalization of the rock wall, aggradation of permafrost will in any case be subjected to climate change and therefore be potential for rock failures (Draebing et al., 2022).

6. Conclusions

In this research study we highlighted the importance of using UAVs for the modelling of ALT. In particular, it has been proved for the first time how the 3D thermography and ATI computation are useful to map the spatial distribution of ALT at very high resolutions in extreme locations, such as a non-easily accessible rock wall of the Italian Central Alps (Gran Zebrù South face).

The validated results showed an ALT in 2022 with >95 % of frequency between 150 and 200 and an average value of 228 cm. Compared to the previous year 2021, we modelled an average ALT increase of 29.3 cm. Classical models (Stefan's solution) underestimated the ALT of almost one order of magnitude and the ALT computation with TDDa resulted to be even thinner than the use of RS TDD. The proposed model is also in contrast to the distribution of permafrost according to APIM.

Since it is expected that there will be less snowfall on the Alps and that south-faced rock walls will steepen with the air warming, it is extremely important to focus the next studies on the magnitudes of these variables for formation and degradation of permafrost: what will be the equilibrium in the future? Will the little snow cover cool the RS during winter favoring permafrost formation or anticipate the snowmelt (long-lasting RS warming) favoring permafrost degradation?

Judging from the ALT variability in just 2 consecutive years, we would expect sudden rock mass wasting on this rock wall as thermal regime consequence that will be a serious risk for the alpine tourism of this area. To prevent similar risks, even low-resolution but widespread UAV surveys on alpine ridges could be treated as mosaic pieces of the same monitoring network that will be addressed to a spatially continuous risk map/scenario, useful for mountaineering and infrastructures.

CRediT authorship contribution statement

Stefano Ponti: Data curation, Methodology, Software, Writing – original draft, Writing – review & editing, Conceptualization, Formal analysis. **Irene Girola:** Data curation. **Mauro Guglielmin:** Conceptualization, Supervision, Writing – review & editing.

Declaration of competing interest

The authors declare that they have no known competing financial interests or personal relationships that could have appeared to influence the work reported in this paper.

Data availability

Data will be made available on request.

References

Albini, S., Battaglia, D., Bellini, G., Bigoni, C., Carminati, E., Ceriani, S., Forcella, F., Gosso, G., Guizzetti, D., Oliva, A., et al., 1994. Alpine deformations and pre-Alpine remnants in the north-eastern Orobic Alps, Southalpine Belt. Quad. Geodin. Alp. Quat. 2, 25–39.

Augustinus, P.C., 1995. Glacial valley cross-profile development: the influence of in situ rock stress and rock mass strength, with examples from the Southern Alps, New Zealand. Geomorphology 14, 87–97. https://doi.org/10.1016/0169-555X(95)00050-X.

Bandfield, J.L., Feldman, W.C., 2008. Martian high latitude permafrost depth and surface cover thermal inertia distributions. J. Geophys. Res. Planets 113, 1–13. https://doi.org/10.1029/2007JE003007.

Biskaborn, B.K., Smith, S.L., Noetzli, J., Matthes, H., Vieira, G., Streletskiy, D.A., Schoeneich, P., Romanovsky, V.E., Lewkowicz, A.G., Abramov, A., Allard, M., Boike, J., Cable, W.L., Christiansen, H.H., Delaloye, R., Diekmann, B., Drozdov, D., Etzelmüller, B., Grosse, G., Guglielmin, M., Ingeman-Nielsen, T., Isaksen, K., Ishikawa, M., Johansson, M., Johannsson, H., Joo, A., Kaverin, D., Kholodov, A., Konstantinov, P., Kröger, T., Lambiel, C., Lanckman, J.P., Luo, D., Malkova, G., Meiklejohn, I., Moskalenko, N., Oliva, M., Phillips, M., Ramos, M., Sannel, A.B.K., Sergeev, D., Seybold, C., Skryabin, P., Vasiliev, A., Wu, Q., Yoshikawa, K., Zheleznyak, M., Lantuit, H., 2019. Permafrost is warming at a global scale. Nat. Commun. https://doi.org/10.1038/s41467-018-08240-4.

Bisset, R.R., Nienow, P.W., Goldberg, D.N., Wigmore, O., Loayza-Muro, R.A., Wadham, J. L., Macdonald, M.L., Bingham, R.G., 2022. Using thermal UAV imagery to model distributed debris thicknesses and sub-debris melt rates on debris-covered glaciers. J. Glaciol. 1–16.

Boeckli, L., Brenning, A., Gruber, S., Noetzli, J., 2012. Permafrost distribution in the European Alps: calculation and evaluation of an index map and summary statistics. Cryosphere 6, 807–820. https://doi.org/10.5194/tc-6-807-2012.

Bommer, C., Phillips, M., Arenson, L.U., 2010. Practical recommendations for planning, constructing and maintaining infrastructure in mountain Permafrost. Permafr. Periglac. Process. 21, 97–104. https://doi.org/10.1002/ppp.679.

Bonnaventure, P.P., Lamoureux, S.F., 2013. The active layer: a conceptual review of monitoring, modelling techniques and changes in a warming climate. Prog. Phys. Geogr. 37, 352–376. https://doi.org/10.1177/0309133313478314.

Buckel, J., Mudler, J., Gardeweg, R., Hauck, C., Hilbich, C., Frauenfelder, R., Kneisel, C., Buchelt, S., Blöthe, J.H., Hördt, A., Bücker, M., 2022. Identifying mountain permafrost degradation by repeating historical ERT-measurements. Cryosphere Discuss. 2022, 1–36. https://doi.org/10.5194/tc-2022-207.

Colombo, R., Pennati, G., Pozzi, G., Garzonio, R., Di Mauro, B., Giardino, C., Cogliati, S., Rossini, M., Maltese, A., Pogliotti, P., Cremonese, E., 2023. Mapping snow density through thermal inertia observations. Remote Sens. Environ. 284, 113323 https://doi.org/10.1016/j.rse.2022.113323.

Corripio, J.G., 2004. Snow surface albedo estimation using terrestrial photography. Int. J. Remote Sens. 25, 5705–5729. https://doi.org/10.1080/01431160410001709002.

D'Agata, C., Bocchiola, D., Maragno, D., Smiraglia, C., Diolaiuti, G.A., 2014. Glacier shrinkage driven by climate change during half a century (1954–2007) in the Ortles-Cevedale group (Stelvio National Park, Lombardy, Italian Alps). Theor. Appl. Climatol. 116, 169–190. https://doi.org/10.1007/s00704-013-0938-5.

Delaloye, R., 2008. Parois glaciaires… parois rocheuses: l'évolution séculaire des grandes faces alpines. In: Klimaveränderungen auf der Spur. Studien des Europäisches Tourismus Instituts an der Academia Engiadina, Samedan, 5, pp. 93–104.

Draebing, D., Krautblatter, M., Dikau, R., 2014. Interaction of thermal and mechanical processes in steep permafrost rock walls: a conceptual approach. Geomorphology 226, 226–235. https://doi.org/10.1016/j.geomorph.2014.08.009.

Draebing, D., Haberkorn, A., Krautblatter, M., Kenner, R., Phillips, M., 2017. Thermal and mechanical responses resulting from spatial and temporal snow cover variability in permafrost rock slopes, Steintaelli, Swiss Alps. Permafr. Periglac. Process. 28, 140–157. https://doi.org/10.1002/ppp.1921.

Draebing, D., Mayer, T., Jacobs, B., McColl, S.T., 2022. Alpine rockwall erosion patterns follow elevation-dependent climate trajectories. Commun. Earth Environ. 3, 1–12. https://doi.org/10.1038/s43247-022-00348-2.

Duvillard, P.A., Ravanel, L., Marcer, M., Schoeneich, P., 2019. Recent evolution of damage to infrastructure on permafrost in the French Alps. Reg. Environ. Chang. 19, 1281–1293. https://doi.org/10.1007/s10113-019-01465-z.

Duvillard, P.A., Magnin, F., Revil, A., Legay, A., Ravanel, L., Abdulsamad, F., Coperey, A., 2021a. Temperature distribution in a permafrost-affected rock ridge from conductivity and induced polarization tomography. Geophys. J. Int. 225, 1207–1221. https://doi.org/10.1093/gji/ggaa597.

Duvillard, P.A., Ravanel, L., Schoeneich, P., Deline, P., Marcer, M., Magnin, F., 2021b. Qualitative risk assessment and strategies for infrastructure on permafrost in the French Alps. Cold Reg. Sci. Technol. 189, 103311 https://doi.org/10.1016/j.coldregions.2021.103311.

Etzelmüller, B., 2013. Recent advances in mountain permafrost research. Permafr. Periglac. Process. 24, 99–107. https://doi.org/10.1002/ppp.1772.

Etzelmüller, B., Guglielmin, M., Hauck, C., Hilbich, C., Hoelzle, M., Isaksen, K., Noetzli, J., Oliva, M., Ramos, M., 2020. Twenty years of European mountain permafrost dynamics-the PACE legacy. Environ. Res. Lett. 15 https://doi.org/10.1088/1748-9326/abae9d.

Etzelmüller, B., Czekirda, J., Magnin, F., Duvillard, P.A., Ravanel, L., Malet, E., Aspaas, A., Kristensen, L., Skrede, I., Majala, G.D., Jacobs, B., Leinauer, J., Hauck, C., Hilbich, C., Böhme, M., Hermanns, R., Eriksen, H.O., Lauknes, T.R., Krautblatter, M., Westermann, S., 2022. Permafrost in monitored unstable rock slopes in Norway-new insights from temperature and surface velocity measurements, geophysical surveying, and ground temperature modelling. Earth Surf. Dyn. 10, 97–129. https://doi.org/10.5194/esurf-10-97-2022.

Evans, S.G., Clague, J.J., 1994. Recent climatic change and catastrophic geomorphic processes in mountain environments. In: Geomorphology and Natural Hazards. Elsevier B.V, pp. 107–128. https://doi.org/10.1016/b978-0-444-82012-9.50012-8.

Forte, E., Santin, I., Ponti, S., Colucci, R.R., Gutgesell, P., Guglielmin, M., 2021. New insights in glaciers characterization by differential diagnosis integrating GPR and remote sensing techniques: a case study for the Eastern Gran Zebrù glacier (Central Alps). Remote Sens. Environ. 267, 112715 https://doi.org/10.1016/j.rse.2021.112715.

Fraser, R.H., Olthof, I., Maloley, M., Fernandes, R., Prevost, C., van der Sluijs, J., Kokelj, S., Lantz, T., Tunnicliffe, J., 2015. UAV photogrammetry for mapping and monitoring of northern permafrost landscapes. Int. Arch. Photogramm. Remote. Sens. Spat. Inf. Sci. 1, 361.

Galibert, G., 1960. L'évolution actuelle des guillemotleft faces nord guillemotright de la haute montagne alpine dans le massif de Zermatt. Revue géographique des Pyrénées et du Sud-Ouest. Sud-Ouest Eur. 31, 133–163.

Galvao, L.S., Vitorello, I., 1995. Quantitative approach in the spectral reflectance-lithostratigraphy of the Wind River and southern Bighorn basins, Wyoming. Int. J. Remote Sens. 16, 1617–1631. https://doi.org/10.1080/01431169508954500.
Gladich, I., Gallai, I., Giaiotti, D.B., Stel, F., 2011. On the diurnal cycle of deep moist convection in the southern side of the Alps analysed through cloud-to-ground lightning activity. Atmos. Res. 100, 371–376. https://doi.org/10.1016/j.atmosres.2010.08.026.
Grechi, G., Fiorucci, M., Marmoni, G.M., Martino, S., 2021. 3D thermal monitoring of jointed rock masses through infrared thermography and photogrammetry. Remote Sens. 13, 1–25. https://doi.org/10.3390/rs13050957.
Guglielmin, M., 2006. Ground surface temperature (GST), active layer and permafrost monitoring in continental Antarctica. Permafr. Periglac. Process. 17, 133–143. https://doi.org/10.1002/ppp.553.
Guglielmin, M., Cannone, N., 2012. A permafrost warming in a cooling Antarctica? Clim. Chang. 111, 177–195. https://doi.org/10.1007/s10584-011-0137-2.
Guglielmin, M., Aldighieri, B., Testa, B., 2003. PERMACLIM: a model for the distribution of mountain permafrost, based on climatic observations. Geomorphology 51, 245–257. https://doi.org/10.1016/S0169-555X(02)00221-0.
Guglielmin, M., Donatelli, M., Semplice, M., Serra Capizzano, S., 2018. Ground surface temperature reconstruction for the last 500 years obtained from permafrost temperatures observed in the SHARE STELVIO Borehole, Italian Alps. Clim. Past 14, 709–724. https://doi.org/10.5194/cp-2017-23.
Guglielmin, M., Ponti, S., Forte, E., Cannone, N., 2021a. Recent thermokarst evolution in the Italian Central Alps. Permafr. Periglac. Process. https://doi.org/10.1002/ppp.2099.
Guglielmin, M., Ponti, S., Forte, E., Cannone, N., 2021b. Recent thermokarst evolution in the Italian Central Alps. Permafr. Periglac. Process. 32, 299–317. https://doi.org/10.1002/ppp.2099.
Guilbert, V., Antoine, R., Heinkelé, C., Maquaire, O., Costa, S., Gout, C., Davidson, R., Sorin, J.L., Beaucamp, B., Fauchard, C., 2020. Fusion of thermal and visible poin clouds: application to the Vaches Noires landslide, Normandy, France. In: The International Archives of the Photogrammetry, Remote Sensing and Spatial Information Sciences-ISPRS Archives, 43, pp. 227–232. https://doi.org/10.5194/isprs-archives-XLIII-B2-2020-227-2020.
Hasler, A., Gruber, S., Haeberli, W., 2011. Temperature variability and offset in steep alpine rock and ice faces. Cryosphere 5, 977–988. https://doi.org/10.5194/tc-5-977-2011.
Heinl, M., Leitinger, G., Tappeiner, U., 2012. Diurnal surface temperature regimes in mountain environments. Phys. Geogr. 33, 344–359. https://doi.org/10.2747/0272-3646.33.4.344.
Hipp, T., Etzelmüller, B., Westermann, S., 2014. Permafrost in alpine rock faces from Jotunheimen and Hurrungane, southern Norway. Permafr. Periglac. Process. 25 (1), 1–13. https://doi.org/10.1002/ppp.1799.
Hrbáček, F., Cannone, N., Kňažková, M., Malfasi, F., Convey, P., Guglielmin, M., 2020. Effect of climate and moss vegetation on ground surface temperature and the active layer among different biogeographical regions in Antarctica. Catena (Amst.) 190. https://doi.org/10.1016/j.catena.2020.104562.
IPCC, 2022. In: Pörtner, H.-O., Roberts, D.C., Tignor, M., Poloczanska, E.S., Mintenbeck, K., Alegría, A., Craig, M., Langsdorf, S., Löschke, S., Möller, V., Okem, A., Rama, B. (Eds.), Climate Change 2022: Impacts, Adaptation, and Vulnerability. Contribution of Working Group II to the Sixth Assessment Report of the Intergovernmental Panel on Climate Change. Cambridge University Press. Cambridge University Press, Cambridge, UK and New York, NY, USA, p. 3056. https://doi.org/10.1017/9781009325844.
Jones, B.M., Tape, K.D., Clark, J.A., Bondurant, A.C., Ward Jones, M.K., Gaglioti, B.V., Elder, C.D., Witharana, C., Miller, C.E., 2021. Multi-dimensional remote sensing analysis documents beaver-induced permafrost degradation, Seward Peninsula, Alaska. Remote Sens. 13 https://doi.org/10.3390/rs13234863.
Jorgenson, M.T., Grosse, G., 2016. Remote sensing of landscape change in permafrost regions. Permafr. Periglac. Process. 27, 324–338. https://doi.org/10.1002/ppp.1914.
Kenner, R., Noetzli, J., Hoelzle, M., Raetzo, H., Phillips, M., 2019. Distinguishing ice-rich and ice-poor permafrost to map ground temperatures and ground ice occurrence in the Swiss Alps. Cryosphere 13 (7), 1925–1941. https://doi.org/10.5194/tc-13-1925-2019.
Kotlarski, S., Gobiet, A., Morin, S., Olefs, M., Rajczak, J., Samacoïts, R., 2023. 21st century alpine climate change. Clim. Dyn. 60, 65–86. https://doi.org/10.1007/s00382-022-06303-3.
Kraaijenbrink, P.D.A., Shea, J.M., Litt, M., Steiner, J.F., Treichler, D., Koch, I., Immerzeel, W.W., 2018. Mapping surface temperatures on a debris-covered glacier with an unmanned aerial vehicle. Front. Earth Sci. (Lausanne) 6, 1–19. https://doi.org/10.3389/feart.2018.00064.
Krautblatter, M., Verleysdonk, S., Flores-Orozco, A., Kemna, A., 2010. Temperature-calibrated imaging of seasonal changes in permafrost rock walls by quantitative electrical resistivity tomography (Zugspitze, German/Austrian Alps). Case Rep. Med. 115, 1–15. https://doi.org/10.1029/2008JF001209.
Kurdel, P., Sedláčková, A.N., Labun, J., 2019. UAV flight safety close to the mountain massif. Transp. Res. Procedia 43, 319–327. https://doi.org/10.1016/j.trpro.2019.12.047.
la Cour Bohr, M., Mähl, P.B., Filsø, S.S., Aagaard, S.P., 2015. Active layer modelling. In: Field and Method Course-Greenland. University of Copenhagen.
Legay, A., Magnin, F., Ravanel, L., 2021. Rock temperature prior to failure: analysis of 209 rockfall events in the Mont Blanc massif (Western European Alps). Permafr. Periglac. Process. 32, 520–536. https://doi.org/10.1002/ppp.2110.
Leonelli, G., Battipaglia, G., Cherubini, P., Saurer, M., Siegwolf, R.T.W., Maugeri, M., Stenni, B., Fusco, S., Maggi, V., Pelfini, M., 2017. Larix decidua δ18O tree-ring cellulose mainly reflects the isotopic signature of winter snow in a high-altitude glacial valley of the European Alps. Sci. Total Environ. 579, 230–237. https://doi.org/10.1016/j.scitotenv.2016.11.129.
Magnin, F., 2015. Distribution et caractérisation du permafrost des parois du massif du Mont Blanc: une approche combinant monitoring, modélisation et géophysique. Université Grenoble Alpes (ComUE).
Magnin, Florence, Krautblatter, M., Deline, P., Ravanel, L., Malet, E., Bevington, A., 2015a. Determination of warm, sensitive permafrost areas in near-vertical rockwalls and evaluation of distributed models by electrical resistivity tomography. Case Rep. Med. 120, 745–762. https://doi.org/10.1002/2014JF003351.
Magnin, F., Deline, P., Ravanel, L., Noetzli, J., Pogliotti, P., 2015b. Thermal characteristics of permafrost in the steep alpine rock walls of the Aiguille du Midi (Mont Blanc Massif, 3842 m a.s.l). Cryosphere 9, 109–121. https://doi.org/10.5194/tc-9-109-2015.
Magnin, F., Josnin, J.Y., Ravanel, L., Pergaud, J., Pohl, B., Deline, P., 2017. Modelling rock wall permafrost degradation in the Mont Blanc massif from the LIA to the end of the 21st century. Cryosphere 11, 1813–1834. https://doi.org/10.5194/tc-11-1813-2017.
Magnin, F., Etzelmüller, B., Westermann, S., Isaksen, K., Hilger, P., Hermanns, R.L., 2019. Permafrost distribution in steep rock slopes in Norway: measurements, statistical modelling and implications for geomorphological processes. Earth Surf. Dyn. 7, 1019–1040. https://doi.org/10.5194/esurf-7-1019-2019.
Maltese, A., Minacapilli, M., Cammalleri, C., Ciraolo, G., D'Asaro, F., 2010. A thermal inertia model for soil water content retrieval using thermal and multispectral images. In: Remote Sensing for Agriculture, Ecosystems, and Hydrology XII, 7824, p. 78241G. https://doi.org/10.1117/12.864672.
Marty, C., Tilg, A.-M., Jonas, T., 2017. Recent evidence of large-scale receding snow water equivalents in the European Alps. J. Hydrometeorol. 18, 1021–1031.
Maset, E., Fusiello, A., Crosilla, F., Toldo, R., Zorzetto, D., 2017. Photogrammetric 3D building reconstruction from thermal images. In: ISPRS Annals of the Photogrammetry, Remote Sensing and Spatial Information Sciences, 4, pp. 25–32. https://doi.org/10.5194/isprs-annals-IV-2-W3-25-2017.
Minacapilli, M., Cammalleri, C., Ciraolo, G., D'Asaro, F., Iovino, M., Maltese, A., 2012. Thermal inertia modeling for soil surface water content estimation: a laboratory experiment. Soil Sci. Soc. Am. J. 76, 92–100. https://doi.org/10.2136/sssaj2011.0122.
Mineo, S., Caliò, D., Pappalardo, G., 2022. UAV-based photogrammetry and infrared thermography applied to rock mass survey for geomechanical purposes. Remote Sens. 14 https://doi.org/10.3390/rs14030473.
Molau, U., Mølgaard, P., 1996. International Tundra Experiment (ITEX) Manual, second ed. Danish Polar Center, Copenhagen.
Montrasio, A., Berra, F., Sciesa, E., Mazzoccola, D., Mair, V., Longhin, M., Gazzola, D., Guglielmin, M., Bini, A., Cariboni, M., et al., 2012. Foglio 024 Bormio. Carta Geologica d'Italia alla scala 1: 50.000.
Myhra, K.S., Westermann, S., Etzelmüller, B., 2017. Modelled distribution and temporal evolution of permafrost in steep rock walls along a latitudinal transect in Norway by CryoGrid 2D. Permafr. Periglac. Process. 28, 172–182. https://doi.org/10.1002/ppp.1884.
Nelson, F.E., Outcalt, S.I., 1987. A computational method for prediction and regionalization of permafrost. Arct. Alp. Res. 19, 279–288.
Nesbit, P.R., Hugenholtz, C.H., 2019. Enhancing UAV-SfM 3D model accuracy in high-relief landscapes by incorporating oblique images. Remote Sens. 11, 1–24. https://doi.org/10.3390/rs11030239.
Nigrelli, G., Chiarle, M., Merlone, A., Coppa, G., Musacchio, C., 2022. Rock temperature variability in high-altitude rockfall-prone areas. J. Mt. Sci. 19 (3), 798–811. https://doi.org/10.1007/s11629-021-7073-z.
Nixon, J.F., 1990. Effect of climatic warming on pile creep in permafrost. J. Cold Reg. Eng. 4, 67–73.
Obu, J., Westermann, S., Bartsch, A., Berdnikov, N., Christiansen, H.H., Dashtseren, A., Delaloye, R., Elberling, B., Etzelmüller, B., Kholodov, A., Khomutov, A., Kääb, A., Leibman, M.O., Lewkowicz, A.G., Panda, S.K., Romanovsky, V., Way, R.G., Westergaard-Nielsen, A., Wu, T., Yamkhin, J., Zou, D., 2019. Northern Hemisphere permafrost map based on TTOP modelling for 2000–2016 at 1 km^2 scale. Earth Sci. Rev. 193, 299–316. https://doi.org/10.1016/j.earscirev.2019.04.023.
Obu, J., Westermann, S., Vieira, G., Abramov, A., Balks, M.R., Bartsch, A., Hrbáček, F., Kääb, A., Ramos, M., 2020. Pan-Antarctic map of near-surface permafrost temperatures at 1 km^2 scale. Cryosphere 14, 497–519.
Oke, T.R., 1987. Boundary Layer Climates. Building and Environment, second ed. Taylor & Francis, London. https://doi.org/10.4324/9780203407219.
Oliva, M., Žebre, M., Guglielmin, M., Hughes, P.D., Çiner, A., Vieira, G., Bodin, X., Andrés, N., Colucci, R.R., García-Hernández, C., Mora, C., Nofre, J., Palacios, D., Pérez-Alberti, A., Ribolini, A., Ruiz-Fernández, J., Sarıkaya, M.A., Serrano, E., Urdea, P., Valcárcel, M., Woodward, J.C., Yıldırım, C., 2018. Permafrost conditions in the Mediterranean region since the Last Glaciation. Earth Sci. Rev. https://doi.org/10.1016/j.earscirev.2018.06.018.
Paige, D.A., 1992. The thermal stability of near-surface ground ice on Mars. Nature 356, 43–45. https://doi.org/10.1038/356043a0.
Paige, D.A., Keegan, K.D., 1994. Thermal and albedo mapping of the polar regions of Mars using Viking thermal mapper observations: 2. South polar region. J. Geophys. Res. 99 https://doi.org/10.1029/93je03429.
Paranunzio, R., Laio, F., Chiarle, M., Nigrelli, G., Guzzetti, F., 2016. Climate anomalies associated with the occurrence of rockfalls at high-elevation in the Italian Alps. Nat. Hazards Earth Syst. Sci. 16, 2085–2106. https://doi.org/10.5194/nhess-16-2085-2016.
Pepin, N., Bradley, R.S., Diaz, H.F., Baraer, M., Caceres, E.B., Forsythe, N., Fowler, H., Greenwood, G., Hashmi, M.Z., Liu, X.D., Miller, J.R., Ning, L., Ohmura, A.,

Palazzi, E., Rangwala, I., Schöner, W., Severskiy, I., Shahgedanova, M., Wang, M.B., Williamson, S.N., Yang, D.Q., 2015. Elevation-dependent warming in mountain regions of the world. Nat. Clim. Chang. https://doi.org/10.1038/nclimate2563.

PERMOS, 2022. In: Noetzli, J., Pellet, C. (Eds.), Swiss Permafrost Bulletin 2021, p. 22. https://doi.org/10.13093/permos-bull-2022. No. 3.

Pirulli, M., 2009. The Thurwieser rock avalanche (Italian Alps): description and dynamic analysis. Eng. Geol. 109, 80–92. https://doi.org/10.1016/j.enggeo.2008.10.007.

Pogliotti, P., Guglielmin, M., Cremonese, E., Morra Di Cella, U., Filippa, G., Pellet, C., Hauck, C., 2015. Warming permafrost and active layer variability at Cime Bianche, Western European Alps. Cryosphere 9, 647–661. https://doi.org/10.5194/tc-9-647-2015.

Ponti, S., Guglielmin, M., 2021. Shore evidences of a high Antarctic Ocean wave event: geomorphology, event reconstruction and coast dynamics through a remote sensing approach. Remote Sens. 13 https://doi.org/10.3390/rs13030518.

Ponti, S., Cannone, N., Guglielmin, M., 2018. Needle ice formation, induced frost heave, and frost creep: a case study through photogrammetry at Stelvio Pass (Italian Central Alps). Catena (Amst.) 164, 62–70. https://doi.org/10.1016/j.catena.2018.01.009.

Ponti, S., Cannone, N., Guglielmin, M., 2021a. A new simple topo-climatic model to predict surface displacement in paraglacial and periglacial mountains of the European Alps: the importance of ground heating index and floristic components as ecological indicators. Ecol. Indic. 120 https://doi.org/10.1016/j.ecolind.2020.106889.

Ponti, S., Pezza, M., Guglielmin, M., 2021b. The development of Antarctic tafoni: relations between differential weathering rates and spatial distribution of thermal events, salts concentration and mineralogy. Geomorphology 373, 107475. https://doi.org/10.1016/j.geomorph.2020.107475.

Ponti, S., Scipinotti, R., Pierattini, S., Guglielmin, M., 2021c. The spatio-temporal variability of frost blisters in a perennial frozen lake along the Antarctic coast as indicator of the groundwater supply. Remote Sens. 13 https://doi.org/10.3390/rs13030435.

Putzig, N.E., Mellon, M.T., Kretke, K.A., Arvidson, R.E., 2005. Global thermal inertia and surface properties of Mars from the MGS mapping mission. Icarus 173, 325–341. https://doi.org/10.1016/j.icarus.2004.08.017.

Qin, Y., Wu, T., Zhao, L., Wu, X., Li, R., Xie, C., Pang, Q., Hu, G., Qiao, Y., Zhao, G., Liu, G., Zhu, X., Hao, J., 2017. Numerical modeling of the active layer thickness and permafrost thermal state across Qinghai-Tibetan Plateau. J. Geophys. Res. Atmos. 122 (21), 11–604. https://doi.org/10.1002/2017JD026858.

Ravanel, L., Deline, P., Lambiel, C., Vincent, C., 2013. Instability of a high alpine rock ridge: the lower Arête des Cosmiques, Mont Blanc Massif, France. Geogr. Ann. Ser. B 95, 51–66. https://doi.org/10.1111/geoa.12000.

Ravanel, L., Magnin, F., Deline, P., 2017. Impacts of the 2003 and 2015 summer heatwaves on permafrost-affected rock-walls in the Mont Blanc massif. Sci. Total Environ. 609, 132–143. https://doi.org/10.1016/j.scitotenv.2017.07.055.

Rico, I., Magnin, F., López Moreno, J.I., Serrano, E., Alonso-González, E., Revuelto, J., Hughes-Allen, L., Gómez-Lende, M., 2021. First evidence of rock wall permafrost in the Pyrenees (Vignemale peak, 3,298 m a.s.l., 42°46′16″N/0°08′33″W). Permafr. Periglac. Process. 32, 673–680. https://doi.org/10.1002/ppp.2130.

Rippin, D.M., Pomfret, A., King, N., 2015. High resolution mapping of supra-glacial drainage pathways reveals link between micro-channel drainage density, surface roughness and surface reflectance. Earth Surf. Process. Landf. 40, 1279–1290. https://doi.org/10.1002/esp.3719.

Riseborough, D., Shiklomanov, N., Etzelmüller, B., Gruber, S., Marchenko, S., 2008. Recent advances in permafrost modelling. Permafr. Periglac. Process. 19, 137–156.

Robertson, E.C., 1988. Thermal properties of rocks. In: Open-File Report. https://doi.org/10.3133/ofr88441.

Samsonov, S.V., Lantz, T.C., Kokelj, S.V., Zhang, Y., 2016. Growth of a young pingo in the Canadian Arctic observed by RADARSAT-2 interferometric satellite radar. Cryosphere 10, 799–810. https://doi.org/10.5194/tc-10-799-2016.

Santin, I., Forte, E., Nicora, M., Ponti, S., Guglielmin, M., 2023. Where does a glacier end? Integrated geophysical, geomorphological and photogrammetric measurements to image geometry and ice facies distribution. Catena (Amst.) 225, 107016. https://doi.org/10.1016/j.catena.2023.107016.

Scaioni, M., Barazzetti, L., Yordanov, V., Azzoni, R.S., Fugazza, D., Cernuschi, M., Diolaiuti, G.A., 2019. Structure-From-Motion Photogrammetry to Support the Assessment of Collapse Risk in Alpine Glaciers, Lecture Notes in Geoinformation and Cartography. Springer International Publishing. https://doi.org/10.1007/978-3-030-05330-7_10.

Scandroglio, R., Draebing, D., Offer, M., Krautblatter, M., 2021. 4D quantification of alpine permafrost degradation in steep rock walls using a laboratory-calibrated electrical resistivity tomography approach. Near Surf. Geophys. 19, 241–260. https://doi.org/10.1002/nsg.12149.

Smith, S.L., O'Neill, H.B., Isaksen, K., Noetzli, J., Romanovsky, V.E., 2022. The changing thermal state of permafrost. Nat. Rev. Earth Environ. https://doi.org/10.1038/s43017-021-00240-1.

Sommer, C., Malz, P., Seehaus, T.C., Lippl, S., Zemp, M., Braun, M.H., 2020. Rapid glacier retreat and downwasting throughout the European Alps in the early 21st century. Nat. Commun. 11, 3209. https://doi.org/10.1038/s41467-020-16818-0.

Soncini, A., Bocchiola, D., Confortola, G., Minora, U., Vuillermoz, E., Salerno, F., Viviano, G., Shrestha, D., Senese, A., Smiraglia, C., Diolaiuti, G., 2016. Future hydrological regimes and glacier cover in the Everest region: the case study of the upper Dudh Koshi basin. Sci. Total Environ. 565, 1084–1101. https://doi.org/10.1016/j.scitotenv.2016.05.138.

van der Sluijs, J., Kokelj, S.V., Fraser, R.H., Tunnicliffe, J., Lacelle, D., 2018. Permafrost terrain dynamics and infrastructure impacts revealed by UAV photogrammetry and thermal imaging. Remote Sens. 10 https://doi.org/10.3390/rs10111734.

Verstraeten, W.W., Veroustraete, F., Van Der Sande, C.J., Grootaers, I., Feyen, J., 2006. Soil moisture retrieval using thermal inertia, determined with visible and thermal spaceborne data, validated for European forests. Remote Sens. Environ. 101, 299–314. https://doi.org/10.1016/j.rse.2005.12.016.

Wegmann, M., Gudmundsson, G.H., Haeberli, W., 1998. Permafrost changes in rock walls and the retreat of alpine glaciers: a thermal modelling approach. Permafr. Periglac. Process. 9, 23–33. https://doi.org/10.1002/(SICI)1099-1530(199801/03)9:1<23::AID-PPP274>3.0.CO;2-Y.

Zhang, T., 2005. Influence of the seasonal snow cover on the ground thermal regime: an overview. Rev. Geophys. https://doi.org/10.1029/2004RG000157.

Zhang, T., Frauenfeld, O.W., Serreze, M.C., Etringer, A., Oelke, C., McCreight, J., Barry, R.G., Gilichinsky, D., Yang, D., Ye, H., Ling, F., Chudinova, S., 2005. Spatial and temporal variability in active layer thickness over the Russian Arctic drainage basin. J. Geophys. Res.D: Atmos. 110, 1–14. https://doi.org/10.1029/2004JD005642.

Zhang, C., Douglas, T.A., Anderson, J.E., 2021. Modeling and mapping permafrost active layer thickness using field measurements and remote sensing techniques. Int. J. Appl. Earth Obs. Geoinf. 102, 102455 https://doi.org/10.1016/j.jag.2021.102455.

Zwieback, S., 2021. Topographic asymmetry across the Arctic. Geophys. Res. Lett. 48, 1–10. https://doi.org/10.1029/2021GL094895.